Stability and synthesis of 2D metals and alloys
a review

Wang, T.; Park, M.; Yu, Q.; Zhang, J.; Yang, Y.

Document Version:
Final Published version, also known as Publisher's PDF, Publisher's Final version or Version of Record

Publication record in CityU Scholars:
Go to record

Citing this paper
Please note that where the full-text provided on CityU Scholars is the Post-print version (also known as Accepted Author Manuscript, Peer-reviewed or Author Final version), it may differ from the Final Published version. When citing, ensure that you check and use the publisher's definitive version for pagination and other details.

Publisher permission
Permission for previously published items are in accordance with publisher's copyright policies sourced from the SHERPA RoMEO database. Links to full text versions (either Published or Post-print) are only available if corresponding publishers allow open access.

Take down policy
Contact lbscholars@cityu.edu.hk if you believe that this document breaches copyright and provide us with details. We will remove access to the work immediately and investigate your claim.

Download date: 28/08/2022
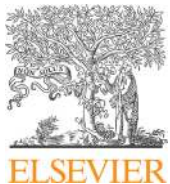
Stability and synthesis of 2D metals and alloys: a review

T. Wang [a], M. Park [a], Q. Yu [a, c], J. Zhang [a], Y. Yang [a, b, *]

[a] Department of Mechanical Engineering, College of Engineering, City University of Hong Kong, Kowloon Tong, Kowloon, Hong Kong, China
[b] Department of Material Science and Engineering, College of Engineering, City University of Hong Kong, Kowloon Tong, Kowloon, Hong Kong, China
[c] Department of Engineering Mechanics, Zhejiang University, Hangzhou, China

ARTICLE INFO

ABSTRACT

As a newcomer to the family of two-dimensional (2D) material, 2D metals and alloys have seen rapid development in recent years because of their unique physical and chemical properties. Unlike free-standing atomistically thin 2D materials, such as graphene, the synthesis of 2D metals and alloys has been focused on either atomistically thin films under nanoscale geometric confinements or freestanding ultrathin films with a thickness ranging from a few to tens of nanometers. In this article, we will first review the recent theoretical works that aimed to understand the thermodynamic stability of 2D metals with or without geometrical confinements. After that, we will focus on the variety of methods that were developed to synthesize 2D metals and/or alloys. Finally, we will briefly discuss some state-of-the-art applications of 2D metals in bioimaging, photothermal therapy, sensing, nanodevices, and catalysis.
© 2020 The Author(s). Published by Elsevier Ltd. This is an open access article under the CC BY license (http://creativecommons.org/licenses/by/4.0/).

1. Introduction

Low-dimensional materials have drawn tremendous attention since the first discovery of graphene [1]. The family of monolayer or two-dimensional (2D) materials has experienced an explosive expansion not only because of the importance of understanding their very existence, but also because of their unprecedented physical and chemical properties as well as a multitude of potential applications [2–5]. Unlike graphene or MoS$_2$ that has intrinsic layered structures, the morphology of metals and alloys are usually considered energetically favored in three-dimension (3D) rather than in 2D because of their non-directional atomic bonding. Despite this apparent difficulty, researchers already found ways to make 2D metals by different means. To date, a number of metallic nanosheets or nanoplates with well-defined shape and size have been successfully synthesized, which were also known as 2D metals and considered as an important kind of 2D materials. Here, it is worth noting that the meaning of 'two-dimensional' is not just restricted to monolayer or atomistically thin materials, but extended to include freestanding ultrathin metallic nanosheets, whose properties depend mostly on their surface [6,7].

Many theoretical works predicted the existence of stable monolayer 2D metals; however, only a few of them were obtained through experiments, either by epitaxially grown on substrates or by confined growth inside the nanopores of 2D templates, such as 2D Fe grown inside nanopores of graphene [8], Ga on Si(111) [9], Sn on Bi$_2$Te$_3$(111) [10], Sb(111) [11], InSb(111) [12], Cu(111) [13], Ag(111) [13], Pb on Pd(111) [14], Bi on SiC(0001) [15], 1T-TaS$_2$ [16], HOPG [17], and Bi$_2$Te$_3$(111) substrates [18]. On the other hand, various methods for the controlled fabrication of freestanding 2D metallic nanosheets were developed in recent years. The solution-based chemical synthesis has been widely used to fabricate various kinds of noble metal nanosheets, nanoplates, or nano-prisms, with well-defined shapes. In addition, new synthesis methods of a pure mechanical origin, such as the polymer surface enabled exfoliation, were also developed, which allows the synthesis of freestanding metallic nanosheets with a much larger lateral scale and a higher degree of chemical complexity. The 2D metals so produced showed excellent performance in catalysis [19,20], bioimaging [21,22], thermal therapy [23], sensing [24], and so on, because of their extended surface area, large lateral-to-thickness aspect ratio, and well-controlled geometry. In this review article, we will start with the discussion of the thermodynamics governing the stability of 2D metals, then proceed to their synthesis and finally to their current applications.

* Corresponding author.
E-mail address: yonyang@cityu.edu.hk (Y. Yang).

2. Thermodynamic stability

Since the first synthesis of monolayer graphene from graphite through mechanical exfoliation in 2004 [1], 2D materials have achieved rapid development in synthesis, characterization, and various novel applications [7,25−28]. For bulk materials with a layered structure, such as graphite, hexagonal boron nitride, transition metal oxides, and transition metal dichalcogenides, the chemical bonding within a layer is covalent, whereas the interlayer bonding is of a weak van der Waals interaction. As a result, the individual atomic layers can be easily separated [1,29−31]. By comparison, for bulk metals with a non-layered atomic structure, at first glance, the strong non-directional metallic bonding in 3D makes it difficult to form 2D metals, especially in a freestanding geometry that contains excessive dangling bonds and, thus, was once considered to be thermodynamically unstable. However, recently, Nevalaita and Koskinen [32] systematically investigated the energetic stability of 45 elemental 2D metal patches using the liquid-drop model, and found that a few metals exhibit an intrinsic 2D stability although their sizes are very small containing only a few atoms. According to the liquid-drop model, the formation energy of an N-atom 3D cluster in the gas-phase without any template is defined as

$$E(N) = \alpha V(N) + \sigma A(N) + E_c(N) \tag{1}$$

where V is the volume; A is the surface area; α and σ are the bulk and surface energy density, respectively; and E_c is the energy arising from the surface curvature. For simplicity, the closely packed, spherical clusters with radius R are selected and the third curvature energy term is neglected. The formation energy per atom for an N-atom 3D cluster in the gas-phase without any template is defined as

$$\varepsilon_{3D}^{gas} = -\varepsilon_{coh}^{3D} + \sigma A(N)\big/N \tag{2}$$

and for a disc-shaped 2D patch is

$$\varepsilon_{2D}^{gas} = -\varepsilon_{coh}^{2D} + \lambda L(N)\big/N \tag{3}$$

where ε_{coh}^{3D} and ε_{coh}^{2D} are the 3D and 2D bulk cohesion, respectively; $A(N) = c_{3D}d_{3D}^2 N^{2/3}$, $c_{3D} = (18\pi)^{1/3} \approx 3.84$, $\lambda =$ the edge energy, $L(N)(= c_{2D}d_{2D}N^{1/2}) =$ the length of the edge, $c_{2D} = (12\pi^2)^{1/4} \approx 3.3$, and d_{3D} and d_{2D} denote, respectively, the 3D and 2D bond length. For most metals, 3D clusters are always more stable than 2D patches and their relative stability increases with increasing N, such as Ir (Fig. 1a), whereas for a few metals, such as Cu, crossover occurs from 2D to 3D at very small N (Fig. 1b), implying the intrinsic 2D stability of certain metal clusters.

To evaluate the relative stability of freestanding 2D and 3D clusters for 45 metals, a dimensionless parameter (Δ) is proposed, the smallness of which represents greater intrinsic 2D stability (Fig. 1c). Most metals with a tendency to form small 2D structures are located at the end of the transition metal series, such as Au, Zn, and Cd. A large number of theoretical studies [33−36] confirmed that small neutral and anionic Au clusters up to a size of 13 atoms prefer to have 2D planar ground-state structures than 3D clusters because of the relativistic effects. Gas-phase ion mobility measurements also revealed the transition of anionic Au clusters from the planar to 3D structures at a size of 12 atoms [37]. In 2004, Rümmeli et al. [8] first reported an experimental synthesis of single-atomic-layer Fe membranes suspended in graphene nanopores (Fig. 2a). These monolayer membranes were made only of Fe atoms with a 2D square lattice structure. Further density-functional theory (DFT) calculations predicted the largest thermodynamically stable Fe membranes to be ~12 atoms wide (3 × 3 nm^2). Later, Pennycook et al. [38] also reported the monolayer MoSe2-stabilized 2D Mo patches, which were small with a size up to 25 nm^2 and retained the close-packed structure of the sandwiched Mo layer in MoSe2 films (Fig. 2b−d). Using molecular dynamics simulations, Koskinen and Korhonen [39] not only found a stable solid 2D Au membrane formed in a graphene nanopore, but also predicted the existence of an unusual 2D liquid Au membranes. All these findings indicate the great potential of perforated 2D materials, especially graphene nanopore, as support to fabricate small-sized 2D metals.

To identify the most stable 2D metal patches grown in graphene nanopores, Nevalaita and Koskinen [32] further investigated the stabilities of 2D patches of 45 metals interacting with a graphene pore. Compared to the gas-phase clusters, the interactions between metal atoms and graphene must be introduced for the 3D cluster within a graphene template, thus the liquid-drop model for the formation energy per atom is

$$\varepsilon_{3D} = -\varepsilon_{coh}^{3D} + \sigma A(N)\big/N + E_{ads}/N \tag{4}$$

analogously, the formation energy for 2D cluster is

$$\varepsilon_{2D} = -\varepsilon_{coh}^{2D} + \left(\lambda - \lambda_{if}\right)L(N)/N \tag{5}$$

where E_{ads} is the cluster adsorption energy and λ_{if} is the metal-graphene interface energy. By comparing the relative stability of 2D and 3D clusters in three different interaction geometries (Fig. 2e), graphene pores significantly improve the stability of 2D metal patches. For example, 2D patches are more energetically favored than 3D clusters with N < 45 for Ir (Fig. 2f) and with N < 125 for Cu (Fig. 2g), demonstrating the ability of perforated graphene to stabilize the 2D metal patches in respectable sizes. Further DFT calculation validated the predictions of the liquid-drop model. Of course, not every element can form a graphene-pore-stabilized 2D structure, several aspects beyond pure energetics need to be considered simultaneously, such as intrinsic relative stability of the 2D metal, commensurability and the resulting strain at the interface, the possibility of carbide formation, and the chemical bonding at the interface. After integrating all these competing viewpoints into a single summative figure of merit, the authors ranked the metals to determine the most stable 2D metal patches and found Cu, Zn, Ag, and Au to be the best candidates (Fig. 2h).

In addition to these small 2D metal patches, many theoretical investigations revealed that if the monolayer metallic atoms are rearranged into a layered crystal structure, that is, away from their corresponding stable 3D bulk structures, to lower the surface energy, freestanding 2D metals may become thermodynamically favorable from both a cohesion energy and lattice dynamics point of view [9,40−54]. The bonding characteristic of these 2D metals, meanwhile, may change accordingly to stabilize these unique 2D structures. Nevalaita and Koskinen [55] systematically investigated the changes in electron density between different structures and found that their chemical bonding characteristic changed from metallic bonds in densely packed hexagonal lattices to covalent bonding as in the honeycomb structure. Fig. 3a shows the typical examples of theoretically proposed stable 2D allotropes of pure metals, including Ag, Au, Cu, Al, Ga, In, Sn, Pb, and Bi, some of which have already been experimentally confirmed, although only on substrates and not in the freestanding form [9−15,17,18,48,56−59]. For example, based on the *ab initio* molecular dynamics simulations, Yang et al. predicted the existence of energetically favorable freestanding 2D Ag [44], Au [45], and Cu [46] monolayer with
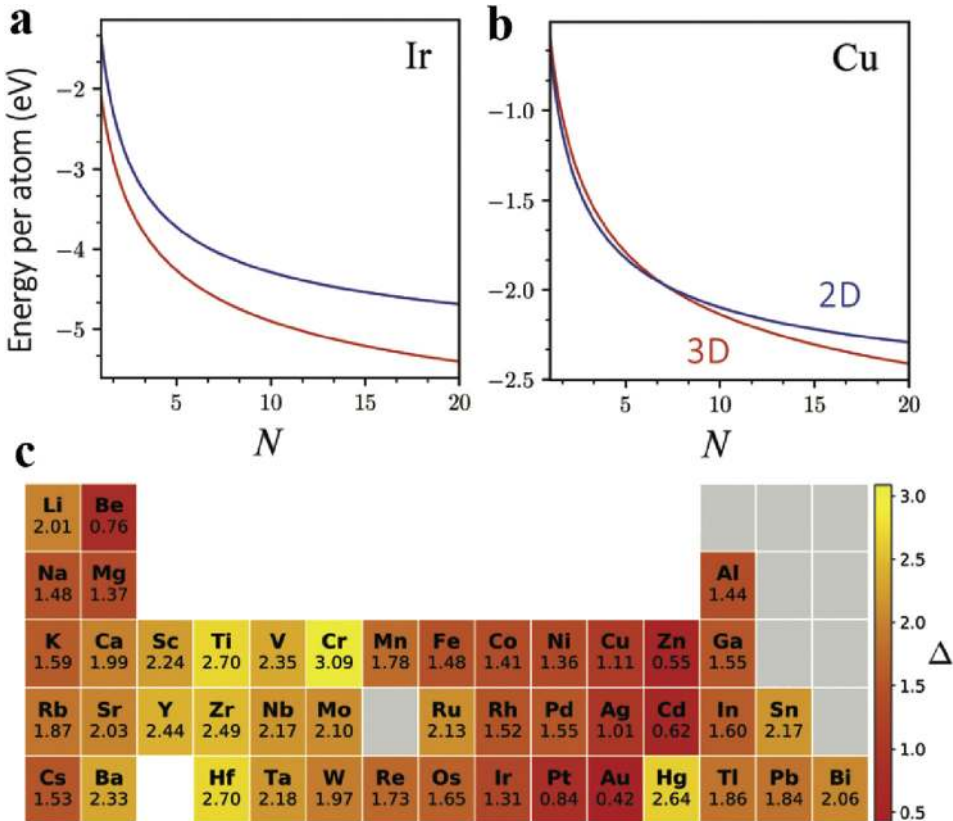
Fig. 1. The relative stability of 2D and 3D clusters in the gas-phase, without the template. Energy per atom for 2D and 3D clusters of (a) Ir and (b) Cu according to the liquid-drop model [Eqs. (2) and (3)]. (c) Dimensionless parameter Δ visualized across the periodic table; the smaller value stands for greater intrinsic 2D stability. Reproduced with permission from Ref. [32]. Copyright © 2019, The Royal Society of Chemistry.

hexagonal close-packed structure instead of 3D bulk face-centered cubic structures (Fig. 3a). The phonon spectra were further calculated to judge the dynamic stability, and the results showed that no imaginary phonon mode was observed, indicating their good dynamic stabilities. Moreover, molecular dynamic annealing simulations revealed that these freestanding 2D metal monolayer films have good thermal stability and preserve their structural integrity at high temperatures.

For the post-transition metals from group III to V in the periodic table (except for the planar honeycomb geometry of graphene), such as Al, Ga, In, Sn, Pb, and Bi, single-atom-thick 2D metals with a buckled honeycomb structure were always predicted to be thermodynamically stable [10,40,41,49−52,61−63], and their 2D geometries were normally termed as aluminene, gallenene, indiene, stanene, plumbene, and bismuthine, respectively. A stable planar honeycomb 2D structure was also predicted for aluminene [47], indiene [61], and bismuthine [43] (Fig. 3a). Ajayan et al. [48] predicted two thermodynamically favored gallenene polymorphs, one with the relaxed planar honeycomb structure obtained from the α-Ga (100) plane and the other with a distorted rhombic lattice directly cleaved along α-Ga (010) direction, which were experimentally confirmed on the SiO$_2$/Si substrate (Fig. 3a−c). Tao et al. [9] also confirmed the stable hexagonal honeycomb gallenene epitaxially grown on Si(111) experimentally and theoretically. Another two possible stanene allotropes were also proposed, one with dumbbell units [53] and the other with a resemblance to a single MoS$_2$ [54] (Fig. 3a), both of which were energetically and dynamically stable from the perspective of their cohesive energy and phonon dispersion relations. In 2015, monolayer stanene was successfully epitaxially grown on a Bi2Te3 substrate (Fig. 3d−f),

which for the first time verified the existence of the theoretically predicted buckled stanene [10]. Afterward, the similar buckled stanene films were synthesized on InSb [12], Sb [11], Au [58], Cu [13], and Ag [59] substrates, all with (111) surfaces. Strong coupling with the Cu and Ag substrates resulted in a nearly flat surface in a honeycomb arrangement. The planar honeycomb plumbene nanosheets were also reported by Yuhara et al. [14] on the Pd (1-x) Pbx (111) substrate (Fig. 3g−i). Bi is a special metal because of its bulk layered rhombohedral structure, which is thus expected to be exfoliated easily to form the 2D structure or bismuthine. Unfortunately, no freestanding monolayer bismuthine was experimentally realized up to date. Theoretically, Zhang et al. [41] found that many 2D bismuthene allotropes were all thermodynamically stable, but only α and β configurations have been experimentally proved [16−18,56,57,64], which exhibits a puckered black-phosphorus-like structure and a buckled rhombohedral structure, respectively (Fig. 3a). *Ab initio* molecular dynamics simulations [63] confirmed that both geometries could keep stable up to 700 K. Apart from a stable monolayer buckled bismuthene grown on a Bi2Te3 [18,56] and HOPG substrates [17], a monolayer bismuthene in the fully planar honeycomb geometry has also been experimentally reported on SiC(0001) surface [15] (Fig. 3j and k), which is energetically stable according to theoretical predictions [43]. So far, only one recent experiment reported the synthesis of self-stabilized, freestanding single-atom-layer Pd nanosheets, however, their thermodynamic stabilities have not been identified yet [65].

If the single or few-nanometer-thick quasi-2D materials with a high aspect ratio are regarded as one type of 2D material, a variety of freestanding and template-supported 2D metals as well as their 2D multimetallic materials have been reported, which exhibit the
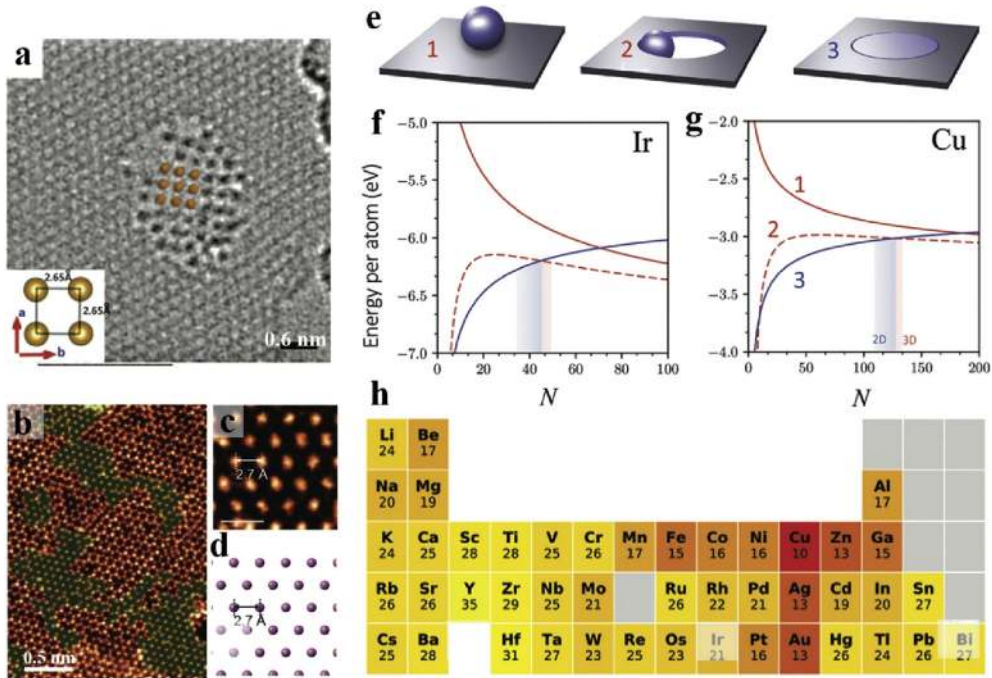
Fig. 2. (a) Low-voltage spherical aberration-corrected transmission electron microscopy (TEM) image of a monoatomic Fe layer with the square unit cell suspected in a graphene pore. The inset highlights the interatomic spacing of the square unit cell. (Reproduced with permission from Ref. [8]. Copyright © 2014, American Association for the Advancement of Science.) (b) Scanning transmission electron microscopy—annular dark field (STEM-ADF) image of as-fabricated monolayer Mo membrane embedded in the monolayer MoSe$_2$ films. Mo membrane regions are highlighted by yellow false color. (c) STEM-ADF image and (d) atomic model of the monolayer Mo membrane, with Mo−Mo distances marked by the white arrows. (Reproduced with permission from Ref. [38]. Copyright © 2018, Wiley-VCH Verlag GmbH & Co. KGaA, Weinheim, Germany.) The relative stability of 2D and 3D clusters interacting with a graphene pore: (e) Different interaction geometries: 3D clusters with on-top (E_{ads}^1) and pore edge (E_{ads}^2) adsorption and 2D patches inside pores ($E_{ads}^3 = \lambda_{if}L$). Energy per atom for the three geometries for (f) Ir ($E_{ads}^1 = 1\ ev, E_{ads}^1 = 15\ ev$, and $\lambda_{if} = 0.94\ ev\ Å^{-1}$) and (g) Cu ($E_{ads}^1 = 1ev, E_{ads}^2 = 15\ ev$, and $\lambda_{if} = 0.62\ ev\ Å^{-1}$) according to Eqs. (4) and (5). The blue/red shading denotes the 2D/3D crossover. (h) Summative figures of merit of 2D stability for the 45 metal candidates. The smallest number represents better 2D stability; numbers are rounded to closest integers. (Reproduced with permission from Ref. [32]. Copyright © 2019, The Royal Society of Chemistry.).

fascinating properties and promising applications in catalysis [27,65−75], sensing [7,25,27,76,77], biomedicine [21,22,27,78,79], surface plasmon resonance [73,80−82], and battery [27,83]. Owing to the large surface energies and the potential strain energy caused by defects [84−86], these ultrathin 2D metallic materials are intrinsically thermodynamically unfavorable and may display single crystal, polycrystal, or even amorphous structure [71,73,87−92]. Thus, to synthesize 2D metallic materials, many strategies in terms of both thermodynamics and kinetics are proposed, such as, through surface-capping [73,80,93−104] or chemical reactions confined in the interlayer space of layered materials [65,71,81,105] or by template-assisted growth [72,75,87,88,106,107]. However, the fundamental issue of the thermodynamic stability of 2D metallic materials remains unclear. Research in the field of 2D metals, including 2D multimetallic materials, is still in its infancy, and systematic studies on the thermodynamic stability of single or a few-atom-layer 2D metals and 2D multicomponent metallic materials are still urgent.

3. Synthesis

Since the first report of the successful fabrication of Au nanoparticles [149], the field of low-dimensional metals has been growing tremendously. To date, chemical syntheses still constitute the major type of methods for making 2D metals. Because of their 'bottom-up' nature, these chemical methods are able to produce 2D metals with controllable geometry and crystalline structure. To be specific, capping agents are usually introduced in these methods in a solution such that the growth of a metallic membrane can be

suppressed in the thickness direction while promoted in lateral directions [27], therefore leading to the formation of single-crystalline nanoplates, nanoprism, or nanosheets with well-defined shapes, such as triangle or hexagon. Through these methods, people already synthesized a variety of 2D elemental metals, such as 2D Au [81,88,93,100,105,109,111,121,128,138, 140,150−165], 2D Ag [98,104,112,116,122,129,164,166−177], 2D Pd [73,127,130,131,133,139,178−180], and so on. More recently, monolayer 2D non-metals, such as graphene, graphene oxides (GOs), graphite, and MoS$_2$, were also used as templates for the confined growth of 2D metals [139,181,182]. However, the shortcomings of the chemical methods are also evident: (1) assembling atoms to build up a 2D membrane has a rather low efficiency of synthesis and also limits the lateral size of the 2D metals so obtained, and (2) the individual synthetic chemical processes used in these chemical methods are usually suitable for only one or two elemental metals. By comparison, the 2D metals fabricated through the 'top-down' methods, such as the mechanical compression [142,143] and polymer surface buckling enabled exfoliation (PSBEE) [92], usually have a large lateral size. Fig. 4 compares the size and geometry of the 2D metals obtained via different methods. The 2D metals synthesized through the typical chemical methods, such as ligands-assisted growth and small-molecule-mediated growth, are usually ~1 μm in width and have an aspect ratio ranging from 10 to 10^2. In contrast, the 2D metals fabricated through the top-down approaches exhibit an aspect ratio in the range from 10^2 to 10^6. As of today, the reported lateral dimension of 2D metals could reach the scale of bulk metals [92]. In this section, we will focus on the different synthesis approaches for 2D metals, including both bottom-up and top-down methods.
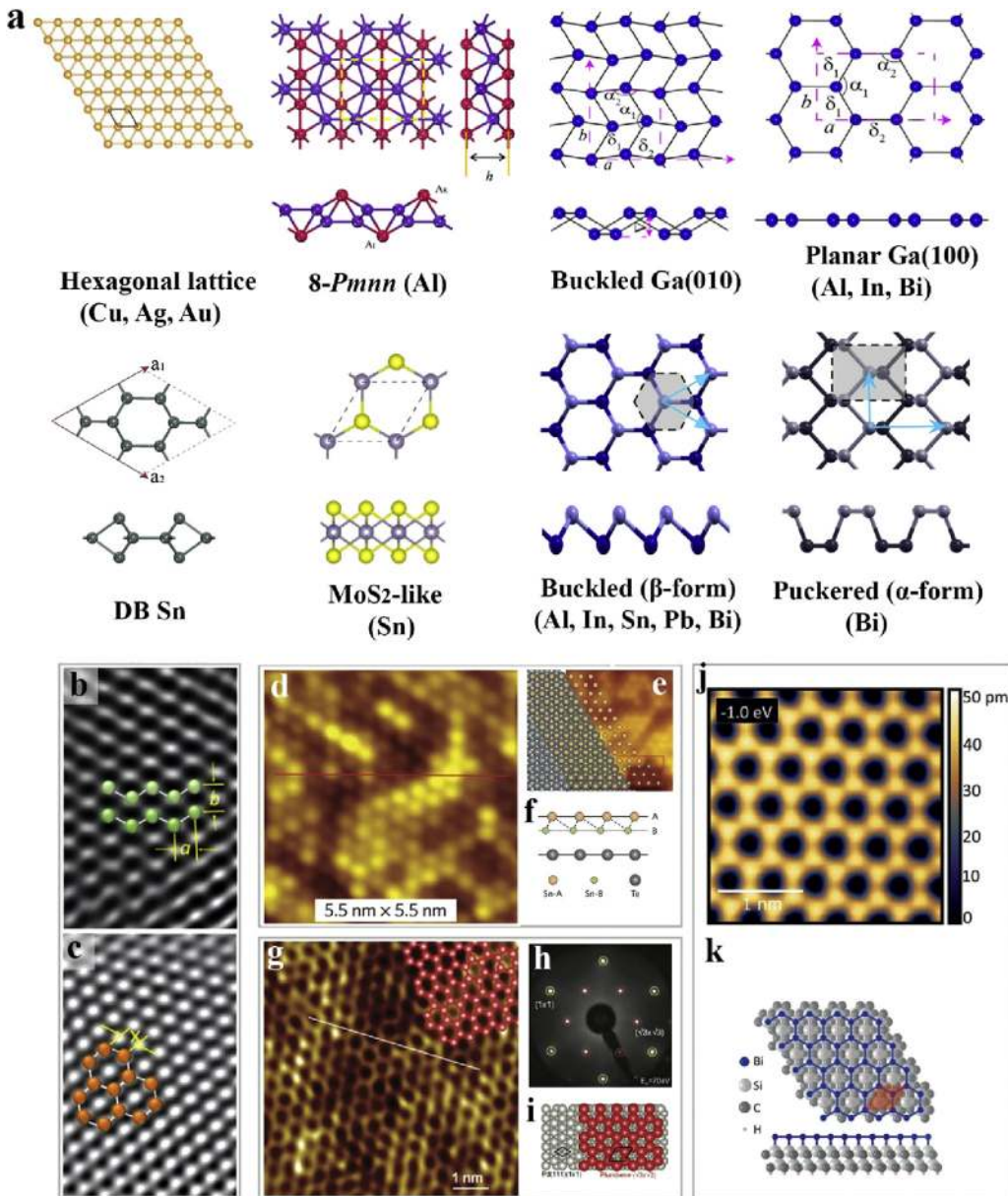
Fig. 3. An atlas of (a) theoretically predicted and (b−k) experimentally realized 2D metals. (a) Stable crystal structures for freestanding monolayer 2D metals predicted by DFT calculations. Image for "hexagonal lattice (Cu, Ag, and Au)" (reproduced with permission from Ref. [45]. Copyright © 2015, the Owner Societies). Image for "8-*Pmnn* (Al)" (reproduced with permission from Ref. [40]. Copyright © 2017, Elsevier B.V.). Images for "Buckled-Ga" and "Planar-Ga" (reproduced with permission from Ref. [48]. Copyright © 2018, The Authors, some rights reserved; exclusive licensee American Association for the Advancement of Science). Images for "DB Sn" (reproduced with permission from Ref. [53]. Copyright © 2014, American Physical Society). Images for "MoS₂-like (Sn)" (reproduced with permission from Ref. [54]. Copyright © 2015, American Physical Society). Images for "α- and β-form" (reproduced with permission from Ref. [60]. Copyright © 2016, American Physical Society). Gallenene (monolayer 2D Ga) via solid-melt exfoliation preparation: high-resolution TEM (HRTEM) images for the gallenene (b) b₀₁₀ and (c) a₁₀₀ sheets, exhibiting a buckled and planar honeycomb structure, respectively (reproduced with permission from Ref. [48]. Copyright © 2018, The Authors, some rights reserved; exclusive licensee American Association for the Advancement of Science). Stanene (monolayer 2D Sn) fabricated by molecular beam epitaxy: (d) atomically resolved scanning tunneling microscope (STM) image of stanene on a Bi₂Te₃ substrate and the corresponding atomic structure mode viewed from (e) top and (f) side, indicating that Sn film grows as a buckled structure (reproduced with permission from Ref. [10]. Copyright © 2020 Springer Nature Limited). Plumbene (monolayer 2D Pd) synthesized by the segregation of Pb atoms from Pd₍₁₋ₓ₎Pbₓ(111) alloys: experimentally (g) STM image and (h) low-energy electron diffraction pattern of plumbene on a Pd(111) substrate. (i) Structural model (top view) of a plumbene overlayer on Pd (111) forming a (√3 × √3)R30° unit cell. Red and gray balls denote Pb and Pd atoms, respectively (reproduced with permission from Ref. [14]. Copyright © 2019, Wiley-VCH Verlag GmbH & Co. KGaA, Weinheim, Germany). Bismuthene (monolayer 2D Bi) epitaxially grown on SiC(0001) substrates: (j) Close-up STM images and (k) structural model of bismuthene on SiC(0001) substrate, confirm the formation of a fully planar honeycomb structure (reproduced with permission from Ref. [15]. Copyright © 2017, The Authors, some rights reserved; exclusive licensee American Association for the Advancement of Science).

3.1. Bottom-up approach

3.1.1. Ligands-assisted growth

Capping ligands are broadly used in the synthesis of 2D metals in a wet chemical environment. A ligand generally consists of an active functional 'head' that can bind with metal atoms or ions with the rest being part of an inert molecule that act as a stabilizer. Generally speaking, capping ligands with long-chain molecules as inert parts results in better steric stabilization [7,27]. Capping agents can either directly bind with individual metal atoms or are
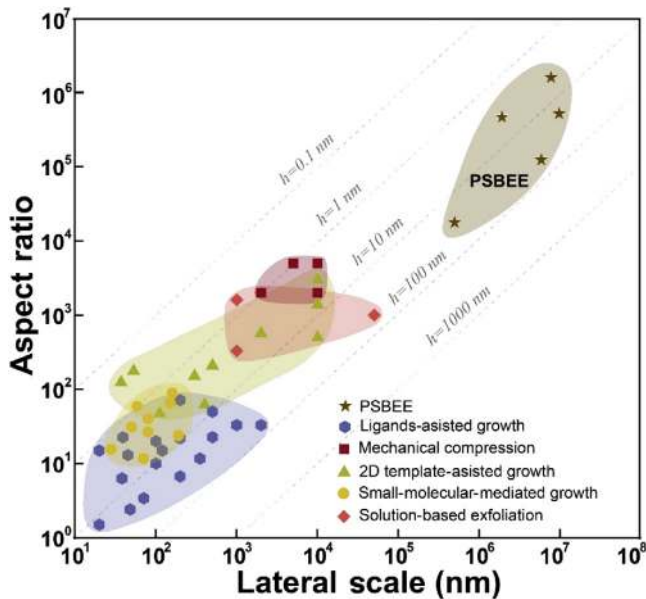
Fig. 4. Comparison of the lateral size versus aspect ratio (thickness-to-lateral scale) for the 2D metals synthesized by different methods. The data points are collected from Refs. [108–125] (ligands-assisted growth), Refs. [73,126–134] (small-molecule-mediated growth), Refs. [81,88,105,135–141] (2D template-assisted growth), Refs. [90,142–144] (mechanical compression), Refs. [145–148] (chemical reduction enabled exfoliation), and Refs. [92] (PSBEE). Note that *h* represents the thickness of the 2D metals. PSBEE, polymer surface buckling enabled exfoliation.

absorbed on thermodynamically favorable crystallized planes. During the growth of 2D metals, the inert parts of the metal–ligand complexes could form a 2D morphology because of a 'soft templating' effect [93,184]. Using this method, 2D metals with the subnanometer thickness were synthesized. For example, Xu et al. [180] designed a pyridinium-type surfactant with a long carbon chain as the capping agent in the synthesis of ultrathin palladium nanosheets (PdNSs). The PdNSs were prepared at 35 °C on a large scale with H_2PdCl_4 as the precursor and ascorbic acid as the reducing agent. As shown in Fig. 5a, the edge length of the nanosheets ranges from 100 to 200 nm. The AFM images and the height profiles shown in Fig. 5b–c indicate that the PdNSs are 8 Å thin, or have a thickness of several atomic layers. With proper stimulates, the shapes of the nanoplates could be easily controlled (Fig. 5d–e). More recently, co-reduction was frequently used to fabricate 2D bimetallic nanosheets (Fig. 5f–h) and even trimetallic nanosheets. Note that the commonly used surfactants for the ligand-assisted growth of 2D metals include poly (vinylpyrrolidone) (PVP) [113,118,122,166,168,176,185], cetyltrimethylammonium bromide (CTAB) [100,121,152], oleylamine [93,121,125], and so on.

3.1.2. Small-molecule-mediated growth

The presence of small molecules or ions, which are usually considered as additives in the solution-based synthetic process, can play an essential role in guiding the anisotropic growth of metallic nanocrystals. Comparing to PVP or other surfactants that consist of long-chain molecule, small molecules or ions sometimes show stronger adsorption capability [27]. Preferential adsorption of different molecules or ions on different facets enables tuning the geometry of the nanocrystal [128]. Carbon monoxides (COs) and halide ions (Cl^-, Br^-, and I^-) are representative additives that are frequently used. CO is extensively used in the synthetic process of Pd nanosheets (Fig. 6a) [73,127,130,131,133,178], accompanied by other surfactants, such as PVP or CTAB. For instance, Zheng et al. [73] successfully synthesized Pd nanosheets with thickness as thin

as 1.8 nm through CO-confined growth. In the synthesis process, palladium acetylacetonate, PVP, and a halide salt were dissolved in a solvent, such as benzyl alcohol, followed by charging of CO to 1 bar. CO was also introduced in a co-reduction synthetic process for freestanding Pd–Pt–Ag ternary alloy nanosheets (Fig. 6b–d) [134]. Different from CO, halide ions were usually used in the mediated growth of Au [128,153] and Ag [129] nanosheets. Wei et al. [128] concluded that Cl^- are ineffective in promoting the anisotropic growth of Au nanocrystals because of its relatively weak interaction with the Au surface. In contrast, Br^- and I^- showed selective adsorption on Au{100} and Au{111}, respectively, modulating the growth of nanoprism or nanoplates along a specific direction. In general, it is considered that the degree of specific adsorption of halide ions on low-index Au surfaces should be ranked in the descending order as: $I^->Br^->Cl^->>F^-$.

3.1.3. 2D templates confined growth

The recent development of single-layered 2D materials has drawn tremendous interests because of their broad potential applications. In recent years, researchers extensively explored the possibility of using these 2D materials as templates for the synthesis of 2D metals, although synthesis of 2D metals in confined layers itself, however, is not a new topic. Dated back to the beginning of this century, researchers had reported the successful synthesis of 2D Pd and Pt in the interlayers of graphite using graphite intercalation compounds as precursor materials [135,136,141]. Among these earliest reports of 2D-templated growth, GO or reduced graphene oxide (rGO) was extensively used for the synthesis of Au nanosheets along with typical surfactants, such as PVP or CTAB, and so on. [88,140,150] (Fig. 6e). In an organic surfactant-free synthesis process (Fig. 6f) recently developed by Yang et al. [182], $PtCl_4^{2-}$ were adsorbed onto the surface of GO in the initial stage because of the existence of the oxygen-containing functional group. In the subsequent steps, Pt nanoparticles as reduced by H_2 aggregate on the GO surface formed Pt nanosheets with specific shapes because of the absence of surfactants (Fig. 6g). Apart from GO or rGO, MoS_2 and indium tin oxide were also used for the synthesis of 2D Au, 2D Ag, 2D Pt, and 2D Pd [138,186]. The concept of the 2D template can be extended to liquid–solid [163] interface or soft templates formed by selected surfactants [81,105]. For instance, Jin et al. [81] reported the successful synthesis of ultrathin Au nanosheets between the confined water layers in a lamellar structured hydrogel. The layered membranes in the hydrogel consisted of a self-assembled non-ionic surfactant hexdecylglyceryl maleate and a non-surfactant sodium dodecyl sulphonate. The Au nanosheets so produced could reach a lateral size as large as tens of micrometers with a thickness around 5 nm (as shown in Fig. 6h–i).

3.2. Top-down approach

3.2.1. Mechanical compression

Taking advantage of good ductility of some elemental metals, researchers reported the successful fabrication of a few kinds of freestanding metallic nanosheets through mechanical compression. Fig. 7a illustrates the formation of Bi nanosheets through the hot pressing of small agglomerates of pristine Bi nanoparticles [143,144]. The AFM and SEM images of the Bi nanosheets shown in Fig. 7b–c indicate a minimum thickness of 2.55 nm and a lateral size at the micrometer scale. Following the same line of thinking, some methods even adopted repetitive folding and rolling to form metal nanosheets [90,142]. For example, Wu et al. [90] applied repetitive rolling and folding on an Ag–Al bilayer and obtained a composite plate with ordered stacking of Ag and Al layers. After
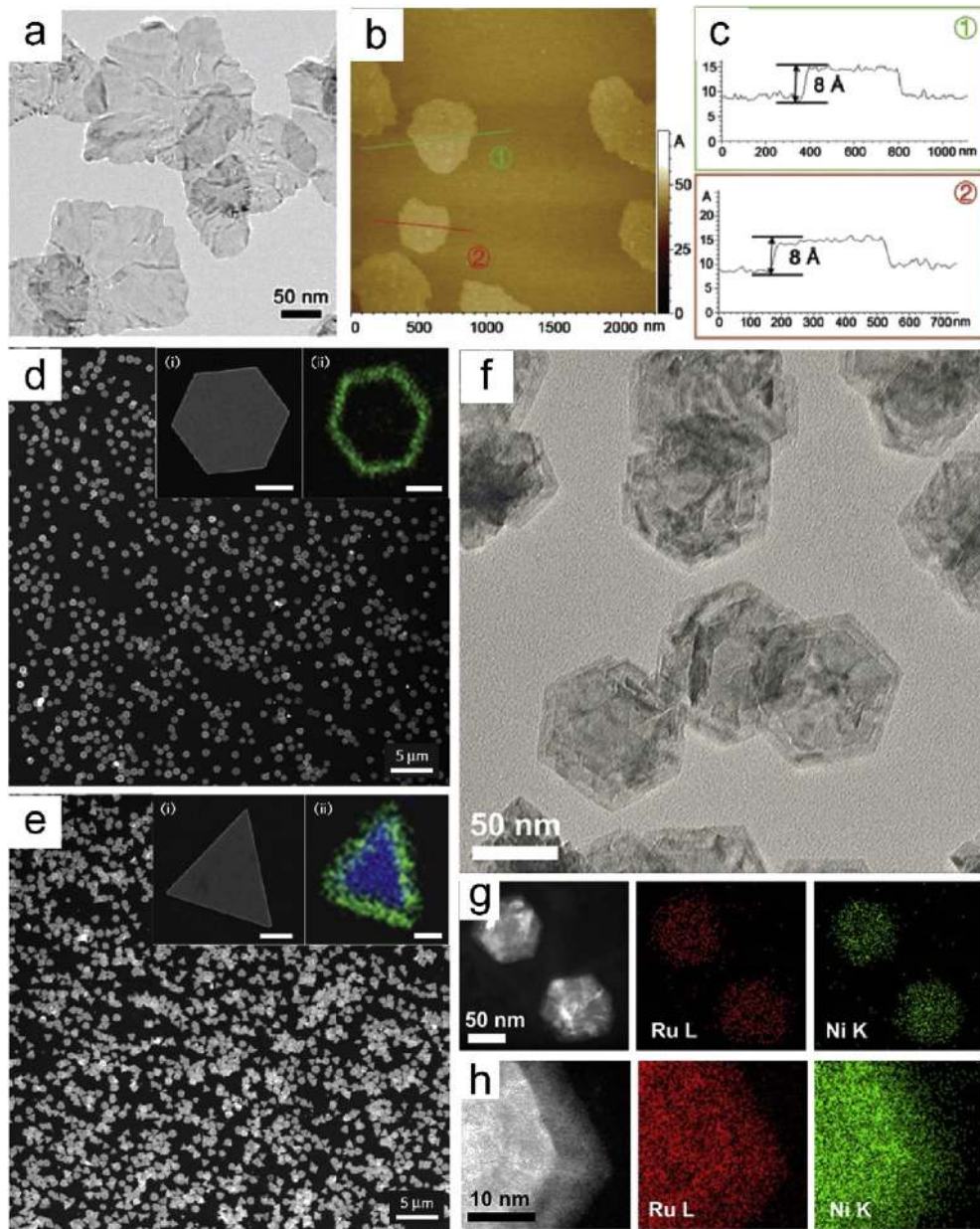
Fig. 5. (a) High-magnification TEM image of Pd nanosheets. (b) Atomic force microscopy (AFM) image of bare Pd nanosheets. (c) Height profiles correspond to the labels ① and ② in (b), respectively. Reproduced with permission from Ref. [180]. Copyright © The Royal Society of Chemistry. (d) SEM image of Au hexagonal nanoprism obtained by the plasmon-driven synthesis after 2 h of irradiation. The insets show a high-magnification SEM image of a single hexagonal nanoprism (i) and a nanoscale secondary ion mass spectrometry (nanoSIMS) image (ii). (e) SEM image of Au triangular nanoprisms obtained. The insets show a high-magnification SEM image of a single triangular nanoprism (i) and a nanoSIMS image (ii). The scale bars in all insets represent 200 nm. Reproduced with permission from Ref. [111]. Copyright © 2016, Springer Nature. (f) Low-magnification TEM image of RuNi nanosheets. (g–h) High-angle annular dark-field (HAADF)-STEM and the corresponding energy dispersive spectroscopy (EDS) elemental mapping images taken from two RuNi nanosheets (g) and the edge region of an individual RuNi nanosheet (h). Reproduced with permission from Ref. [183]. Copyright © 2019, Elsevier Ltd.

selective etching of one kind of metal layers, freestanding Ag or Al nanosheets were obtained. The obtained metal nanosheets showed a thickness of less than 10 nm and a lateral size at the micrometer scale. Similar rolling and folding procedures were also applied to the Al−graphene system and resulted in the successful synthesis of 2D Al with a thickness of ~3 nm [142]. As mechanical compression offers a plausible method to continuously reduce the thickness of bulk materials with significant yield efficiency; however, it only works effectively on a few elemental metals with remarkable ductilities, such as Ag, Al, Au, Ni, Pt, In, Bi, and so on. Notably, there is no control of the geometry of the nanosheets produced by the current mechanical compression methods.

3.2.2. Solution-based exfoliation

Different from most metals, Sb with gray allotrope has a graphene-like layered structure, which allows 2D Sb to be fabricated through exfoliation like graphene. Recently, Yang et al. [148] developed a fabrication method to obtain freestanding Sb nanosheets through liquid-phase exfoliation of bulk Sb powder in isopropyl alcohol (Fig. 7d). The size of the Sb nanosheets so produced ranges from 400 nm to a few micrometers with a thickness around 4 nm. A similar method may be applied to pure metals that do not have layered structures. Matsumoto et al. [145] reported successful preparation of Pt nanosheets by exfoliating the layered Pt precursor materials followed by electrochemical reduction. By adjusting the

reduction conditions, monolayer Pt nanosheets were obtained. Through a similar method, ultrathin Ru nanosheets were also obtained by reducing the exfoliated RuO_2 nanosheets [147].

3.2.3. PSBEE

Surface instability on a stressed soft substrate with metallic coatings was extensively studied for surface patterning [187−189]. Recently, Wang et al. [92] developed a new method based on PSBEE, which enables the fabrication of large-scale freestanding 2D metals and alloys. As shown in Fig. 8a, the typical fabrication process of PSBEE includes the following steps: (1) preparation of a Polyvinyl Alcohol (PVA) substrate, (2) film deposition on the PVA, and (3)

peeling off of the film from the PVA substrate. This method was proved applicable not only to elemental metals, but also to chemically complex alloys such as metallic glass and high entropy alloys such as ZrCuAlNi and $FeCoNiCrNb_{0.5}$ (Fig. 8b−c). Meanwhile, it could be well extended to fabricating ceramic nanosheets, such as TiO_2 and SiC. The lateral size of the 2D metals so produced could reach the centimeter scale with the thickness around tens of nanometers (Fig. 8d). The fabrication is mainly based on a pure mechanical process, which involves crack initiation and propagation at the film−PVA interface. Once immersed in water, the dry PVA substrate would absorb water and start to swell, which, however, is constrained by the upper metal/ceramic film. The
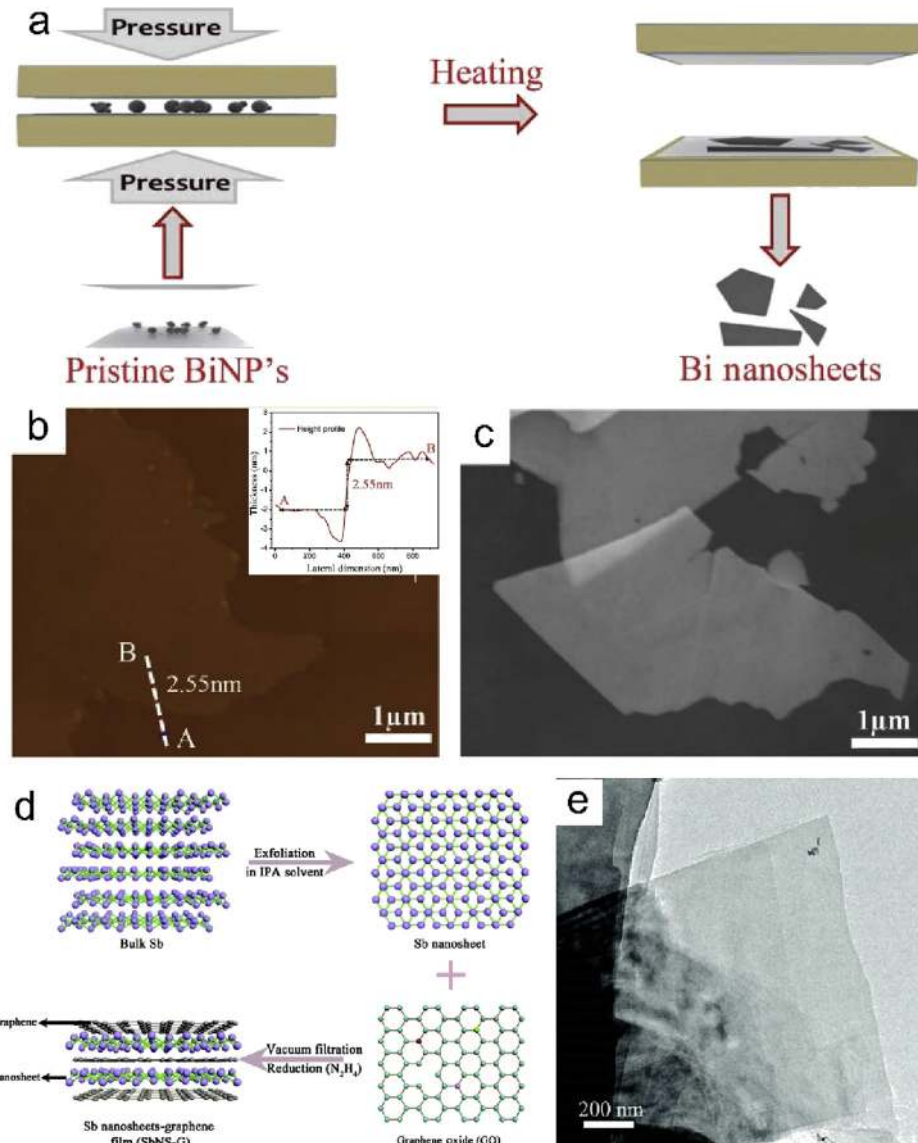
Fig. 7. (a) A schematic diagram illustrating the fabrication process of Bi nanosheets (BiNSs) using pristine Bi nanoparticles via the facile hot-pressing method. (b) AFM image of a large area BiNSs on Si/SiO$_2$ substrate. The inset shows the height profile diagram of a Bi nanosheet marked by 'A–B'. (c) SEM images of BiNSs transferred to carbon tape directly from Si/SiO$_2$ substrate. Reproduced with permission from Ref. [143]. Copyright © 2017, Wiley-VCH Verlag GmbH & Co. KGaA, Weinheim, Germany. (d) Schematic illustration of the fabrication process of Sb nanosheets-graphene (SbNS-G) film. (e) Typical TEM images of Sb nanosheets. Reproduced with permission from Ref. [148]. Copyright © 2017, Wiley-VCH Verlag GmbH & Co. KGaA, Weinheim, Germany.

constraint from the film imposes compression stress on the PVA substrate and leads to surface wrinkling and ultimately to interfacial fracture [92].

In principle, the thickness of the 2D metals/ceramics fabricated via PSBEE is governed by the thermodynamics of film deposition. For magnetron sputtering, according to Zhang et al. [190], both sputtering parameters and target compositions affect whether a deposited film is formed by adatoms or by atomic clusters. In such a case, the minimum thickness of the 2D metals obtained through PSBEE could be related to the typical size of the individual 'patches' or 'islands' formed by the accumulation of atoms or atomic clusters right after they 'land' on the PVA substrate [191]. In theory, a complete solid film is formed once these 'patches' or 'islands' grow into contact. According to the literature [192,193], if the PSBEE method was based on magnetron sputtering, we would estimate that the minimum thickness of non-porous 2D metals formed via adatom deposition, mostly for elemental metals, should be less

than 10 nm; by comparison, this minimum thickness increases to ~10 nm or even more for 2D non-porous chemically complex alloys formed via cluster deposition [194,195]. If the deposited film thickness is less than the minimum thickness because of insufficient deposition time, excessive porosities or vacancies may appear in the 2D metals and alloys fabricated through PSBEE.

Aside from regular planar nanosheets, PSBEE allows the fabrication of nanosheets with controlled shape and size through the use of deposition masks. In Ref. [92], Wang et al. successfully fabricated 2D metals with the shape of circle, square, and hexagon, as shown in Fig. 8e–g. In addition, our recent results show that the PSBEE method is capable of fabricating multilayered nanosheets with patterned interlayers, as seen in Fig. 9. These new interesting results could bring new applications in ultrathin flexible electronics.

The current results revealed that the 'bottom-up' approaches, such as the wet-chemical methods, are versatile in synthesizing
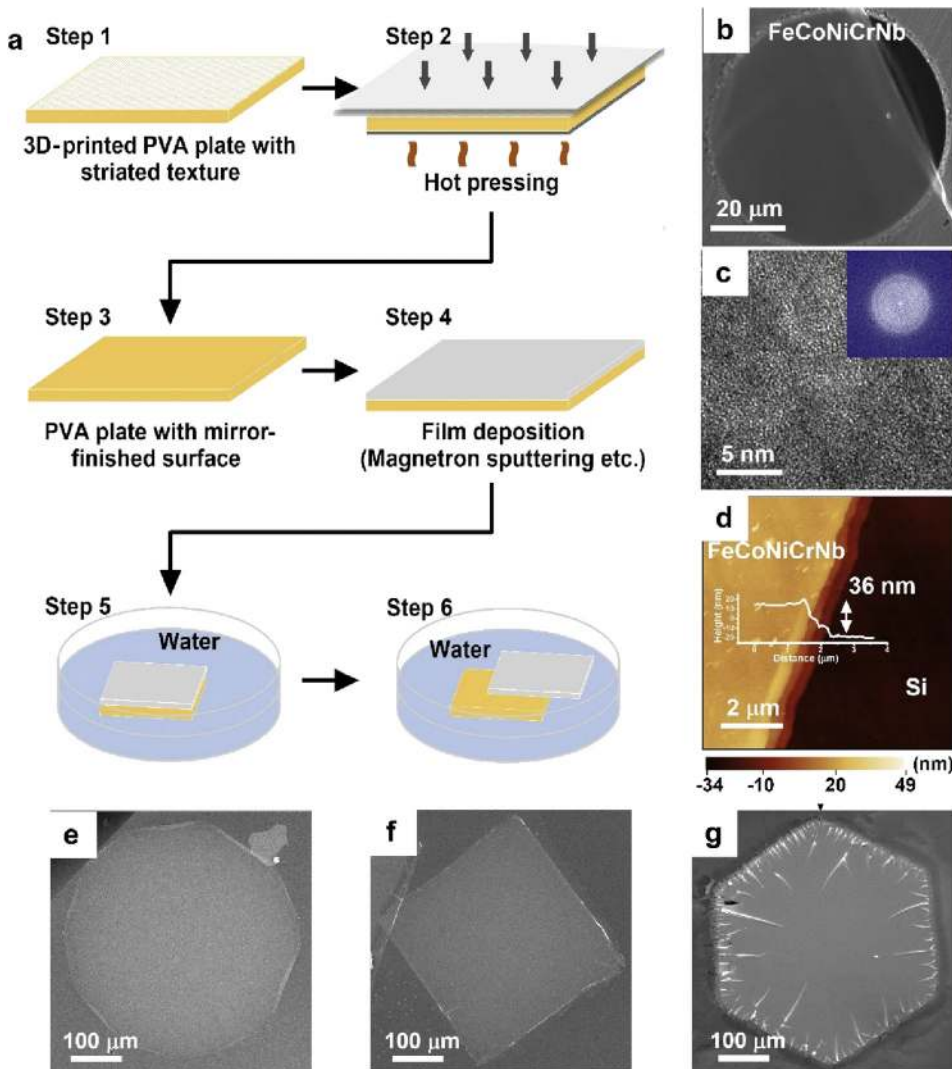
Fig. 8. (a) Schematic illustration of the fabrication process of 2D metals based on PSBEE, (b) SEM, (c) high-resolution TEM, and (d) AFM images of 2D FeCoNiCrNb obtained via PSBEE. The insets of (c) and (d) are the FFT pattern of the corresponding HRTEM image and the line-scan profile across the edge. (e–g) SEM images of the round, square, and hexagon-shaped 2D FeCoNiCrNb fabricated via the masked deposition. Reproduced with permission from Ref. [92]. Copyright © 2020, Elsevier Ltd. All rights reserved.

single-crystalline nanosheets of elemental metals. However, most of the results were obtained mainly for laboratory use and the capability of mass production is yet to be demonstrated for industrial applications. Although it seems that the top-down approaches may have a higher yield than the bottom-up approaches in the fabrication of 2D metals, further research efforts are needed for the mass production of 2D metals.

4. Properties and applications

In recent years, 2D metals have attracted tremendous interest because of their novel optical, physical, and chemical properties [196]. It is the high surface-to-volume ratio, sheet-like structure, and high electron mobility that contribute to the distinct properties of 2D metals, making them promising candidates in future applications. First, sheet-like structures facilitate the coupling between 2D metals and an electromagnetic field, thereby leading to localized surface plasmon resonance (LSPR). In general, LSPR indicates collective oscillation of free electrons in resonance with the electromagnetic radiation at a certain excitation frequency, which is determined by shape, size, and component of metallic

nanostructures. Given some special sheet-like structure and a relatively large lateral size, 2D metals showed broad plasmon absorption in the near-infrared (NIR) region, which is distinct from 0D and 1D metallic nanostructures [27]. As NIR lights have an excellent tissue penetration ability, 2D metals with NIR LSPR are attractive for bioengineering, such as photothermal therapy [23,73,162,197] and bioimaging [21–23,198–200]. In addition, the lateral size of 2D metals could be easily altered by changing the synthesis details [23,162]. As the LSPR absorption peak changes with the size of metal nanostructures, 2D metals usually possess a tunable LSPR absorption peak by changing their lateral size. For example, Fuente et al. [162] reported that the LSPR band of Au nanoprisms was tuned in the NIR region as the size of the nanoprisms changes, enabling the tailoring of LSPR.

Second, the high surface-to-volume ratio results in a high surface energy of 2D metals. Owing to the high density of coordinatively unsaturated atoms and the corresponding large surface area, 2D metals are highly favorable for surface-related applications [201]. Particularly, 2D noble metals were widely studied as a catalyst in various reactions, including hydrogen evolution reaction (HER), oxygen evolution reaction (OER), and so on. Third, shape
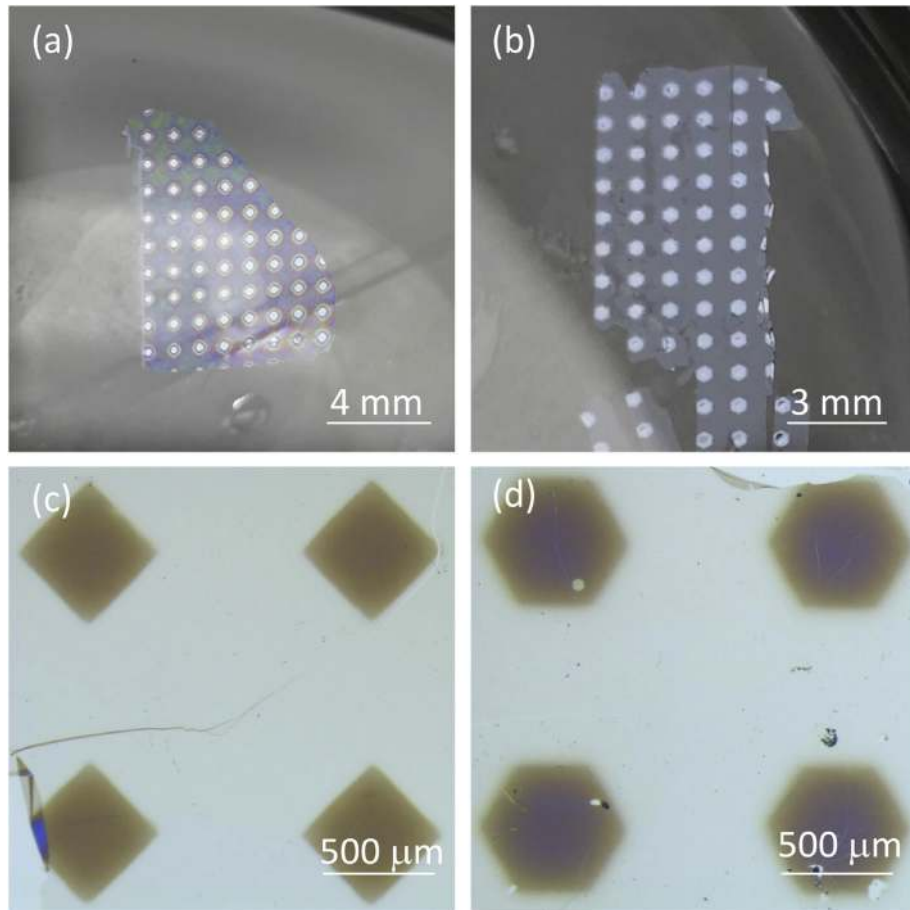
Fig. 9. (a—b) Photos of multilayered nanosheets with patterned interlayer floating on the water surface. (c—d) Optical images of the multilayered nanosheets transferred onto the Si surface.

anisotropies can easily come along with 2D structures, which was found to enhance the magnetic anisotropy feature of metal nanostructures [202]. As anisotropic magnetic properties are the prerequisite for ferromagnetic hysteresis of metals, which could be used in magnetic memory devices [27], 2D nanostructures of magnetic metals (Fe, Co, and Ni) were demonstrated to possess an enhanced magnetic anisotropy, while their isotropic nanoparticles and bulks are usually superparamagnetic at room temperature [203].

4.1. Biomedical engineering

4.1.1. Photothermal therapy

Photothermal therapy is a treatment that generates local hyperthermia *in vivo* to selectively kill targeted cancer cells. The photothermal therapy uses phototherapeutic agents to generate hyperthermia from electromagnetic waves, preferably from NIR lights, which have an excellent tissue penetration ability. 2D metals, such as 2D Au [23,162], were demonstrated to be an excellent candidate material because of their biocompatibilities and strong LSPR absorption in the NIR region. For example, Fuente et al. [162] reported the synthesis and modification of Au nanoprisms (NPRs) with photothermal functions. The LSPR band was altered along the NIR region by tuning the size of the Au NPRs (Fig. 10a—e). The biocompatibility and photothermal stability of the Au NPRs were enhanced after functionalization with heterobifunctional PEG and 4-aminophenyl β-D-glucopyranoside chains, which made the Au NPRs a promising photothermal agent. Zhou

et al. [23] reported an effective method to tailor the plasmon mode of Au triangular nanoprisms by tuning their shape (Fig. 10f). By tuning the plasmon band into one resonant with incident light, the Au triangular nanoprisms exhibited better performance in killing Hela cancer cells, compared to Au nanoprisms without tuning.

Besides 2D Au, 2D Pd also displayed excellent photothermal properties, such as biocompatibilities and photothermal stability. Zheng et al. [73] reported a facile synthesis method for hexagonal Pd nanosheets (NSs) and examined its photothermal performance. Under 10 min NIR laser irradiation, the temperature of the palladium solution with a concentration of 27 ppm increased from 28 °C to 48.7 °C (Fig. 10g). The Pd NSs maintained its sheet-like morphology after 30 min irradiation of 2 W, 808 nm laser, demonstrating an excellent photothermal stability. Impressively, ~100% of liver cancer cells were killed via the photothermal effect caused by the Pd NSs after 5 min of irradiation with an 808-nm laser, indicative of an excellent cell-killing efficiency (Fig. 10h—i). The same group [197] also altered the morphology feature of the Pd NSs by coating them with silica, to promote their entrance into cells. With the increased sheet thickness and positive charges on the sheet surface, the photothermal cell-killing efficiency of the Pd NSs was highly improved.

4.1.2. Bioimaging

According to the literature [21—23,198—200], the sensitivity and selectivity of various bioimaging techniques could be enhanced by the use of 2D metals, which enables tunable light absorption and easy surface modification. Noble metals, such as Ag, Au, and Pd
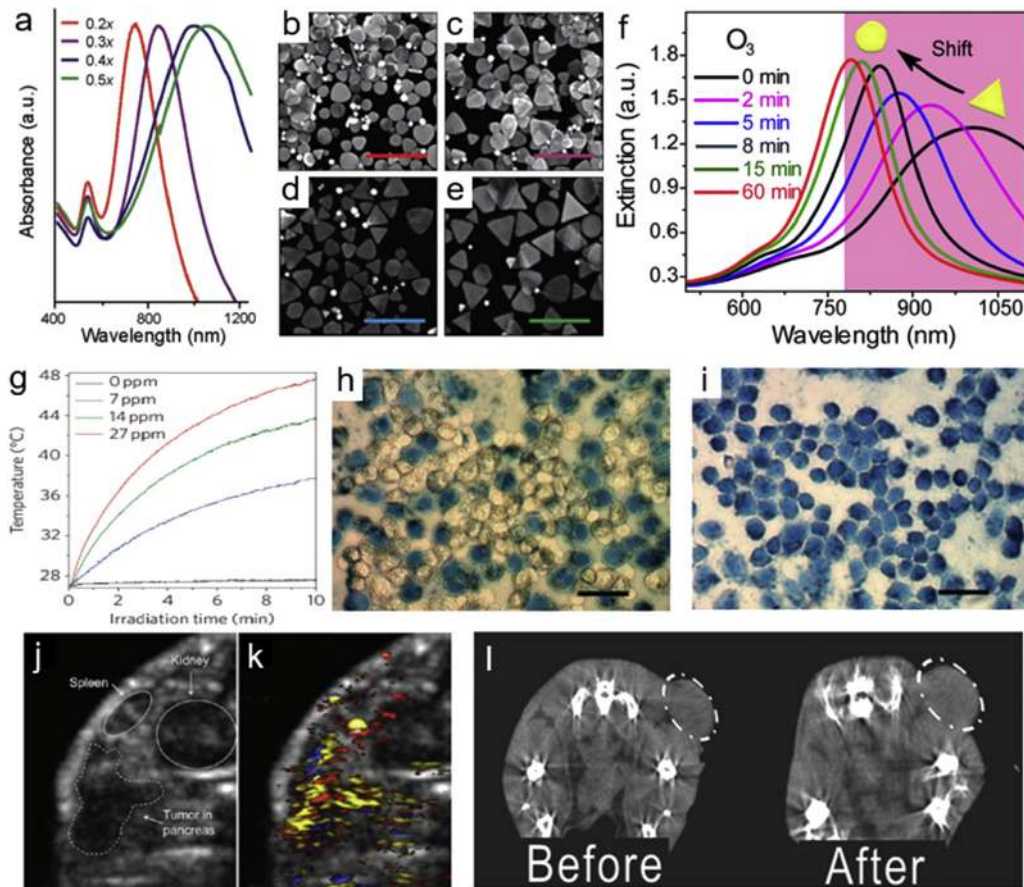
Fig. 10. (a) UV−vis−NIR spectra of the resulting preparations as the volume of the second addition of reductant increases, that is, 0.2×, 0.3×, 0.4×, and 0.5×. (b−e) SEM images of NPRs with an increasing average edge length corresponding to the preparations where the volume of the second addition of reductant was 0.2× (b), 0.3× (c), 0.4× (d), and 0.5× (e); scale bar is 500 nm in all cases. Adapted with permission from Ref. [162]. Copyright © 2012, American Chemical Society. (f) Time-dependent UV−vis extinction spectra of GTNPs when exposed to O₃ (75 ppm) for different periods. The dipole plasmon mode of GTNPs blue-shifts from 1,004 nm to 790 nm in the NIR region (as shown as the red region). The insets show the shape transformation of the gold triangular nanoprism (GTNPs) with the shift of their plasmon mode. Adapted with permission from Ref. [23]. Copyright © 2015, The Royal Society of Chemistry. (g) The plot of temperature vs. time recorded at different concentrations of Pd nanosheets under laser irradiation. (h and i) Micrographs of human hepatoma cells after (h) 2 min and (i) 5 min of irradiation by a 1-W laser. Dead cells are stained in blue. Adapted with permission from Ref. [73]. Copyright © 2011, Nature Publishing Group. (j and k) 2D cross-sections of an orthotopic pancreatic tumor in a nude mouse model. The ultrasound (US) image (j) shows the anatomical features, whereas the ultrasound and photoacoustic (USPA) image (k) shows the molecular accumulation of a-(EGFR) epidermal growth factor receptor conjugated nanoplates (yellow), oxygenated blood (red), and deoxygenated blood (blue). Image dimensions are 14.5 × 11.8 mm. Adapted with permission from Ref. [21]. Copyright © 2011, American Chemical Society. (l) *In vivo* cross-sectional CT images of mice before and after Pd@Au-(PEG) polyethylene glyc. Adapted with permission from Ref. [199]. Copyright © 2014, John Wiley & Sons, Inc.

[21−23,198−200], were extensively studied as a potential contrast agent for bioimaging, particularly for photoacoustic (PA) imaging, in which acoustic waves are generated by a photothermal effect and converted into imaging signals.

Emelianov et al. [21] synthesized Ag nanoplates (NPs) using the biocompatible methods and introduced them as a novel PA imaging contrast agent. Antibody-conjugated Ag nanoplates showed a significant accumulation in pancreatic cancer cells *in vitro* due to receptor-mediated endocytosis. Furthermore, the antibody-conjugated Ag NPs could be visualized in the PA imaging of a mouse with orthotopic pancreatic cancer. The imaging contrast of the tumor region was enhanced (Fig. 10j−k), demonstrating the ability of Ag NPs to selectively enhance the contrast of a specific region. The same group [198] also reported silica-coated Au NPs as a potential PA contrast agent, displaying a sustained and strong PA signal in a sentinel lymph node mapping *in vivo*.

Besides PA imaging, 2D metals were also used in other bioimaging techniques, such as computed tomography (CT) imaging [199], optoacoustic tomography [200], optical coherence imaging [23], and two-photon-induced luminescence [22]. Zheng et al. [199] demonstrated the potential application of core-shell Pd@Au

NPs for both PA and CT imaging. Enhancement of signal intensity was observed 24 h after the injection of Pd@Au NPs during *in vivo* PA imaging and CT imaging (Fig. 10l). Cui et al. [200] used PEGylated Au nanoprisms as signal amplifiers in multispectral optoacoustic tomography. These results indicated that the PEGylated Au nanoprisms were able to provide high-resolution imaging signals, with more fitting light absorption profiles and fewer toxicity than other plasmonic materials.

4.1.3. Sensing

In general, the LSPR absorption peak of metal nanostructures or 2D metals changes when the dielectric constant (refractive index RI) of their surrounding environment is altered. LSPR-based sensing is thus achieved by combining this attribute of 2D metals with complementary molecular identification techniques. In LSPR-based sensing, biological or chemical species are sensed by monitoring the plasmon band shift of 2D metals when the target analyte binds to its surface. Ag- and Au-based metal nanostructures have been most studied in their sensing ability for various biological molecules [24,119,165,204−207].

Zamborini et al. [24] reported a highly sensitive detecting ability of Au nanoplates for human IgG. Au nanoplates showed a red-shift of 22 nm up to 68 nm when they were edge-functionalized with human anti-IgG, which was 4−8 times greater than the shift of Au nanospheres. The human anti−IgG-functionalized Au nanoplates successfully detected 10 pg/mL of human IgG by showing a large red-shift (45 nm) of the LSPR peak, when they were exposed to IgG solution. Kim et al. [208] reported that Ag nanoplates showed a color change induced by LSPR shift when they were aged with styrene-4-sulfonate at room temperature. In addition, color changes of Ag nanoplate solution were found when the Ag nanoplate was aged with potassium persulfate. The degree of blue-shift of final colors was dependent on external temperatures, indicating that the Ag nanoplates could be applied to colorimetric sensing of the temperature.

4.2. Catalysis

4.2.1. Oxygen reduction reaction

Oxygen reduction reaction (ORR) is important for the commercialization of fuel cells and metal-air batteries. Development of ORR, however, has been hindered by its sluggish reaction kinetics, and high cost and poor durability of present commercial catalysts. 2D metal/alloy nanostructures were found to have good performance as ORR catalysts. Ding et al. [209] synthesized ultra-thin core-shell Pd@Pt monolayer. The core-shell Pd@Pt monolayer exhibited an activity of 0.438 A/cm_{Pt}^2 and a mass activity of 0.717 A/mg_{Pt} at the potential of 0.9 V (vs. reversible hydrogen electrode [RHE]) in O_2-saturated 0.1 M $HClO_4$ aqueous solution, reaching 3.4 and 6.6 times that of the commercial Pt/C (Fig. 11a). Bard et al. [212] discovered that elastic strain affects the ORR activity of Pt, that is, compressive strains improved the ORR activity. Huang et al. [20] reported that biaxially strained PtPb@Pt core-shell nanoplates supported on the commercial carbon displayed excellent ORR

performance in aqueous solution. The specific activity could be 33.9 times that of the commercial Pt/C. According to their DFT calculations, the stable Pt (110) facets exposed on the surface of PtPb@Pt core-shell nanoplates had large tensile strains, which were beneficial for optimizing the Pt−O bond strength. Shaojun et al. [213] prepared intermetallic Pd_3Pb square nanoplates (SNP) with a tunable crystalline orientation. The dependence of catalytic activity on crystalline orientation was noticed. Mass activity of the intermetallic Pd_3Pb SNP was 0.78 A/mg at 0.9 V versus RHE in an alkaline condition, which was 7.1 times larger than that of the commercial Pt/C. Recently, Chen et al. [214] synthesized wrinkled Pt−Pd nanosheets and found that the freestanding $Pd_{19}Pt_1$ nanosheet had superior activity toward ORR. The half-wave potential of $Pd_{19}Pt_1$ was 0.949 V (vs. RHE), which was 72 mV more positive than that of Pt/C.

4.2.2. Hydrogen evolution reaction

H_2 is a highly efficient and environmentally friendly fuel source. Water splitting is considered as one of the most promising techniques to generate H_2. Hydrogen evolution reaction (HER) occurs at cathode of the water splitting process. To date, Pt is considered as the most promising catalyst for HER reaction. But its high cost and scarcity have hindered its widespread application in HER. A great deal of effort has been performed to alloy Pt with cheap metals, or to develop a non-precious metal catalyst. Zheng et al. [210] tested the HER catalytic performance of PtCu alloy nanosheets and found that the PtCu alloy nanosheets needed smaller overpotential for HER than PtCu nanoparticles or Pt black. PtCu alloy nanosheets needed overpotential of 55 mV to reach the current density of 100 mA/cm^2, whereas the PtCu nanoparticles and Pt black needed an overpotential of 72 and 111 mV (Fig. 11b). Nanfeng et al. [19] prepared a 3D PdCu structure made up of numerous PdCu nanosheets, and the 3D PdCu nanosheet built structure was found to have exceptional catalytic properties for both HER and the
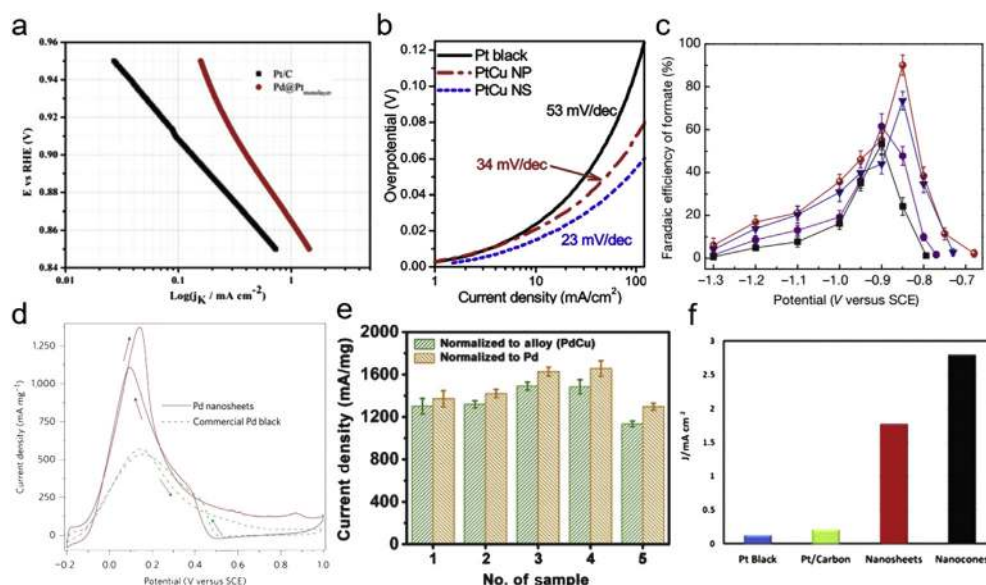

Fig. 11. (a) The area-specific kinetic current densities (j_k) for Pd@Pt$_{monolayer}$ and commercial Pt/C. Adapted with permission from Ref. [209]. Copyright © 2015, The Royal Society of Chemistry. (b) Tafel plots obtained with PtCu nanosheets (NS), PtCu nanoparticles (NP), and Pt black catalysts as indicated without IR correction . Adapted with permission from Ref. [210]. Copyright © 2016, Wiley-VCH Verlag GmbH & Co. KGaA, Weinheim, Germany. (c) Faradaic efficiencies of formate at each given potential for 4 h. The error bars in (c) represent the standard deviations of five independent measurements of the same sample. Adapted with permission from Ref. [94]. Copyright © 2016, Springer Nature. (d) The CV curves were recorded in an aqueous solution containing 0.5 M H_2SO_4 and 0.25 M HCOOH at a scan rate of 50 mV/s⁻. Edge size of palladium nanosheets, 41 nm; palladium black from Aldrich (47 m^2/g). Adapted with permission from Ref. [73]. Copyright © 2010, Springer Nature. (e) PdCu NSs samples peak current densities of ethylenediamine-treated samples 1−5 for FAO. Adapted with permission from Ref. [117]. Copyright © 2017, Wiley-VCH Verlag GmbH & Co. KGaA, Weinheim, Germany). (f) Graphical charts of the specific activities of all the catalysts. Adapted with permission from Ref. [211]. Copyright © 2013, American Chemical Society.

oxidation of alcohol. In a basic medium in 1 M KOH, the over-potential of PdCu nanosheets to reach a current density of 10 mA/cm^2 is 106 mV, which is lower than that of PdCu nanoparticles, Pd nanosheets, and Pd black. Wang et al. [215] reported that the tri-metallic PtAgCo ultrathin nanosheets had higher electrocatalytic activity and durability for HER than the commercial Pt/C catalyst. Very recently, Feng et al. [216] synthesized trimetallic PtRhCo petal-assembled alloyed nanoflowers (PtRhCo PAANFs) with a one-pot solvothermal method, which exhibited superior activity and durability for HER reaction in the alkaline electrolyte. The Tafel slope of the PtRhCo PAANFs (48 mV/dec) is smaller than that of the commercial Pt/C (61 mV/dec), and the normalized chro-noamperometric plot at −0.07 V only shows a smaller attenuation of 7.6% after testing for 12 h under alkaline conditions, demon-strating that suitable content of Rh in the PtRhCo alloy would significantly boost the catalytic durability.

4.2.3. Oxygen evolution reaction

Oxygen evolution reaction (OER) plays an important role in both water splitting process and greenhouse gas (CO_2) reduction. With the increasing concerns in environmental issues and clean energy sources, a highly efficient OER reaction is desired nowadays. However, the sluggish kinetics has been limiting the reaction rate of OER. A great deal of efforts have been dedicated to synthesizing or preparing more efficient OER catalysts [94,217−219]. Huang et al. [218] prepared 3D Ir superstructures made up of ultrathin Ir nanosheets, who had 3D accessible active sites, large surface area, and proper layer distance. The obtained 3D Ir superstructures possess unexceptional OER catalytic properties in both alkaline and acidic conditions, which is better than the Ir nanoparticles. On the other hand, the development of CO_2 reduction catalysts focuses mainly on the Faradaic efficiency and selectivity toward value-added carbon compounds. Freestanding Co nanosheets with four atomic layers were prepared by Xie et al. [94], who found that partially oxidized Co nanosheets had excellent activity and selec-tivity for the CO_2 reduction reaction (Fig. 11c). The OER perfor-mance of the partially oxidized Co nanosheets was better than that of pure Co nanosheets, the partially oxidized bulk Co, and the bulk Co metal.

4.2.4. Oxidation reaction of organic molecules

Direct liquid fuel cells are promising energy devices that have a lower operating temperature and less pollution than conventional energy devices. Among various oxidation reactions of organic molecules, formic acid oxidation reaction (FAO) is regarded as a representative energy source because of its efficient and clean en-ergy supply. 2D metals were demonstrated to have outstanding catalytic properties toward FAO. Particularly, noble metals such as

Pd and Pt and their alloys are widely used as a catalyst for FAO. Wang et al. [220] synthesized one-atom-thick multimetallic PtCu nanosheets with an outer Pd-based alloy shell with doping of other metals. All these PtCu nanosheets unfolded higher catalytic activity for FAO than commercial Pd/C. PtCu@PdIr showed the highest specific activity (1.46 mA/cm^2), which was 8.6 times that of com-mercial Pd/C (0.17 mA/cm^2). In another research of Wang's group [221], 2D Pt−Ag ultrathin NSs were fabricated, and also showed a high specific activity (1.8 mA/cm^2) and mass activity toward FAO. In Zheng's work [73], Pd nanosheets have revealed excellent catalytic activity for FAO as compared to the commercial Pd black. Pd nanosheets showed a maximum current density of 1,380 mA/mg_{Pd} at the peak potential of 0.14 V (vs. saturated calomel elec-trode) for FAO, which is 1.5 times higher than that of commercial Pd black (Fig. 11d). Zhang et al. [117] prepared a series of PdCu alloy NSs with tunable Cu/Pd atomic ratios. They all showed highly enhanced catalytic activity for FAO after the post-treatment with ethylenediamine as compared to other Pd-based catalysts. Particu-larly, the PdCu alloy nanosheets with Cu/Pd atomic ratio of 0.19 unfolded the highest current density, reaching 1,656 mA/mg_{Pd} at the peak potential of 0.12 V (vs. Ag/AgCl) in the FAO (Fig. 11e).

Besides FAO, 2D metals and alloys also demonstrated excellent catalytic properties of the oxidation reaction of alcohols, such as ethanol oxidation reaction (EOR) and methanol oxidation reaction (MOR). For example, Wang's group [211] fabricated PtCu nanocones and nanosheets and used them as catalysts for EOR. PtCu nano-cones exhibited superior catalytic activity, which is about 22 and 14 times higher than that of Pt black and Pt/C, respectively. PtCu nanosheets also showed catalytic activity, which is almost 14 and 9 times higher than that of Pt black and Pt/C (Fig. 11f). Zheng et al. [19] demonstrated that the 3D PdCu alloy nanosheets have superior activity and stability for the EOR when the molar ratio between Pd and Cu is 45/55. Catalytic stability of 3D $Pd_{45}Cu_{55}$ alloy nanosheets was also demonstrated, retaining 96% of the initial activity after 2 h of stability test at 0.7 V (vs. RHE).

4.3. Nanodevice and electronics

Magnetic properties of 2D metals highly depend on their thickness, shape, and nanostructure [202]. Ferromagnetic 2D metals or metallic nanomaterials have a potential application in magnetic memory devices (Fig. 12a). 2D metals, such as Fe, Co, and Ni, with shape anisotropy have been demonstrated to have enhanced magnetic anisotropy, which could finally enhance the ferromagnetic hysteresis [125,132,203,223−225]. For example, Li et al. [203] reported that Co and Ni nanoplatelets with a shape anisotropy exhibited enhanced coercivities and blocking tempera-ture. The coercivity of Co nanoplatelets was 218 Oe (or 176 Oe) with
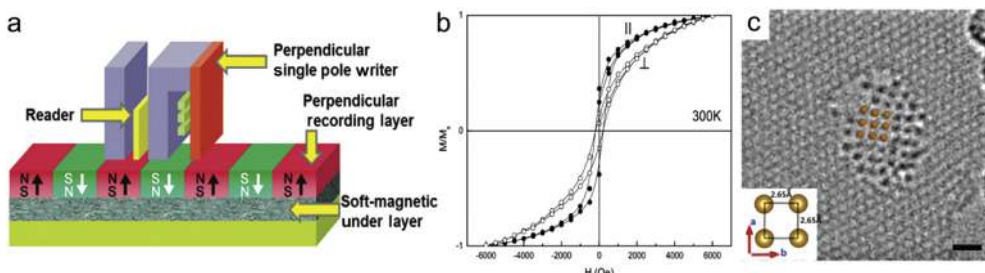

Fig. 12. (a) Schematic of a perpendicular magnetic recording media with ferromagnets. Adapted with permission from Ref. [222]. Copyright © 2015, Wiley-VCH Verlag GmbH & Co. KGaA, Weinheim, Germany. (b) The hysteresis loops of the cobalt nanoplatelets with the magnetic field applied parallel and perpendicular to the nanoplatelets at 300 K, respectively. M/M_s indicates the magnetization (M) normalized by the saturated magnetization (M_s). Adapted with permission from Ref. [203]. Copyright © 2007, American Chemical Society. (c) low-voltage spherical aberration-corrected transmission electron microscope (LVACTEM) micrograph of a monoatomic Fe layer with the square unit cell. The inset highlights the interatomic spacing of the square unit cell. Scale bar, 0.6 nm. Adapted with permission from Ref. [8]. Copyright © 2014, American Association for the Advancement of Science.

the applied magnetic fields parallel (or perpendicular) to the nanoplatelets at 300 K, which is significantly larger than that of bulk Co and the Co spheres (Fig. 12b). Ni nanoplatelets also showed an enhanced coercive force, reaching 120 Oe at 300 K. These results demonstrate the ability of these 2D metallic nanostructures to serve as ferromagnets in memory devices. Single-atom layers of metals also received considerable attention because of their novel magnetic properties. The unsaturated coordination of the atoms of single-atom layers leads to the enhancement of the magnetic moment [226]. Rümmeli et al. [8] reported the formation of the crystalline single-atom layer of Fe, which was suspended across perforations in the graphene (Fig. 12c). The first-principle calculations showed that the magnetic moment of single-atom-layer Fe is ~50% higher than that of bulk BCC Fe. In addition, a large perpendicular magnetic anisotropy arises from the different spin-orbit coupling in the ferromagnetic layer [227]. Application of single-atom-layer metals with such magnetic characteristics is promising for reducing the size of magnetic memory devices and increasing the data-storage density.

Because of the excellent electrical properties of the 2D metals, it is reasonable to consider that the 2D metals could have great use in various kinds of electronics, especially the flexible electronics that have seen rapid development in the past few years. In general, one may adopt the elastomeric stamp printing technique [228] and use the solution mixed with 2D metals as ink to print the circuits. Ahn et al. have demonstrated the feasibility of fabricating arrays of high-electron-mobility transistors and metal−oxide−semiconductor field-effect transistors with the use of GaN bars and Si nanoribbons, respectively [229]. Recent first-principle DFT calculation indicates that it is possible to replace the Si nanoribbons with antimonene [230] and tinene [51].

5. Summary

In summary, according to the liquid-drop energy model [32], only a few metals possess intrinsic 2D stability under the gas-phase condition but their in-plane size is limited. Further atomistic calculations showed that the stability of 2D metals could be significantly improved if confined within the pores in a graphene, which agreed with the experimental results [8,38]. Atomistic simulations also showed that the formation of freestanding 2D metals is possible with a rearranged crystal structure distinct from the corresponding bulk structure [9,40−54], which was also validated by experiments [10−13,58,59].

Aside from atomistic thin 2D metals, various bottom-up and top-down methods were developed to synthesize freestanding ultrathin 2D metal and alloys. At the present time, the chemistry-based synthesis method plays a major role in making 2D metals owing to its good control of the shape of the 2D metals so produced. However, it has several shortcomings, including the low production efficiency, limited lateral size, and restricted chemical composition of the 2D metals. By comparison, the physics-based method, such as the PSBEE [92], enables the fabrication of large-sized 2D metals and alloys with complex chemical compositions.

Benefiting from their novel chemical and physical properties, 2D metals were already used in a few applications, from biomedical engineering, catalysis, to memory devices. However, challenges still remain, including an in-depth understanding of thermodynamic stability of 2D metals and alloys as their chemical compositions become more complicated, and a better control of the thickness, morphology, and shape of 2D metals and alloys such that their applications can be broadened in the years to come. Overall, we believe that, with the development of new processing methods for 2D metals, those capable of mass-producing 2D metals with tunable size, shape, and chemical composition will become popular in the future research and applications.

References

[1] K.S. Novoselov, Science (80-.) 306 (2004) 666−669.
[2] Y. Xu, Z. Lin, X. Huang, Y. Liu, Y. Huang, X. Duan, ACS Nano 7 (2013) 4042−4049.
[3] A. Gupta, T. Sakthivel, S. Seal, Prog. Mater. Sci. 73 (2015) 44−126.
[4] R. You, Y. Liu, Y. Hao, D. Han, Y. Zhang, Z. You, Adv. Mater. 32 (2020) 1901981.
[5] I.W. Frank, D.M. Tanenbaum, A.M. van der Zande, P.L. McEuen, J. Vac. Sci. Technol. B Microelectron. Nanom. Struct. 25 (2007) 2558.
[6] H. Zhao, X. Chen, G. Wang, Y. Qiu, L. Guo, 2D Mater. 6 (2019), 032002.
[7] C. Tan, X. Cao, X.-J. Wu, Q. He, J. Yang, X. Zhang, J. Chen, W. Zhao, S. Han, G.-H. Nam, M. Sindoro, H. Zhang, Chem. Rev. 117 (2017) 6225−6331.
[8] J. Zhao, Q. Deng, A. Bachmatiuk, G. Sandeep, A. Popov, J. Eckert, M.H. Rummeli, Science (80-.) 343 (2014) 1228−1232.
[9] M.-L. Tao, Y.-B. Tu, K. Sun, Y.-L. Wang, Z.-B. Xie, L. Liu, M.-X. Shi, J.-Z. Wang, 2D Mater. 5 (2018), 035009.
[10] F. Zhu, W. Chen, Y. Xu, C. Gao, D. Guan, C. Liu, D. Qian, S.-C. Zhang, J. Jia, Nat. Mater. 14 (2015) 1020−1025.
[11] J. Gou, L. Kong, H. Li, Q. Zhong, W. Li, P. Cheng, L. Chen, K. Wu, Phys. Rev. Mater. 1 (2017), 054004.
[12] C.-Z. Xu, Y.-H. Chan, P. Chen, X. Wang, D. Flötotto, J.A. Hlevyack, G. Bian, S.-K. Mo, M.-Y. Chou, T.-C. Chiang, Phys. Rev. B 97 (2018), 035122.
[13] J. Deng, B. Xia, X. Ma, H. Chen, H. Shan, X. Zhai, B. Li, A. Zhao, Y. Xu, W. Duan, S.-C. Zhang, B. Wang, J.G. Hou, Nat. Mater. 17 (2018) 1081−1086.
[14] J. Yuhara, B. He, N. Matsunami, M. Nakatake, G. Le Lay, Adv. Mater. 31 (2019) 1901017.
[15] F. Reis, G. Li, L. Dudy, M. Bauernfeind, S. Glass, W. Hanke, R. Thomale, J. Schäfer, R. Claessen, Science (80-.) 357 (2017) 287−290.
[16] K. Yamada, S. Souma, K. Yamauchi, N. Shimamura, K. Sugawara, C.X. Trang, T. Oguchi, K. Ueno, T. Takahashi, T. Sato, Nano Lett. 18 (2018) 3235−3240.
[17] F. Song, J.W. Wells, Z. Jiang, M. Saxegaard, E. Wahlström, ACS Appl. Mater. Interfaces 7 (2015) 8525−8532.
[18] T. Hirahara, G. Bihlmayer, Y. Sakamoto, M. Yamada, H. Miyazaki, S. Kimura, S. Blügel, S. Hasegawa, Phys. Rev. Lett. 107 (2011) 166801.
[19] X. Zhao, L. Dai, Q. Qin, F. Pei, C. Hu, N. Zheng, Small 13 (2017) 1602970.
[20] L. Bu, N. Zhang, S. Guo, X. Zhang, J. Li, J. Yao, T. Wu, G. Lu, J.-Y. Ma, D. Su, Science (80-.) 354 (2016) 1410−1414.
[21] K.A. Homan, M. Souza, R. Truby, G.P. Luke, C. Green, E. Vreeland, S. Emelianov, ACS Nano 6 (2012) 641−650.
[22] Y. Jiang, N.N. Horimoto, K. Imura, H. Okamoto, K. Matsui, R. Shigemoto, Adv. Mater. 21 (2009) 2309−2313.
[23] X. Jiang, X. Liu, P. Tang, W. Li, H. Zhong, Z. Zhou, J. Zhou, RSC Adv. 5 (2015) 80709−80718.
[24] S.R. Beeram, F.P. Zamborini, ACS Nano 4 (2010) 3633−3646.
[25] N.R. Glavin, R. Rao, V. Varshney, E. Bianco, A. Apte, A. Roy, E. Ringe, P.M. Ajayan, Adv. Mater. 32 (2020) 1904302.
[26] W. Tao, N. Kong, X. Ji, Y. Zhang, A. Sharma, J. Ouyang, B. Qi, J. Wang, N. Xie, C. Kang, H. Zhang, O.C. Farokhzad, J.S. Kim, Chem. Soc. Rev. 48 (2019) 2891−2912.
[27] Y. Chen, Z. Fan, Z. Zhang, W. Niu, C. Li, N. Yang, B. Chen, H. Zhang, Chem. Rev. 118 (2018) 6409−6455.
[28] X. Kong, Q. Liu, C. Zhang, Z. Peng, Q. Chen, Chem. Soc. Rev. 46 (2017) 2127−2157.
[29] M. Osada, T. Sasaki, J. Mater. Chem. 19 (2009) 2503.
[30] J.N. Coleman, M. Lotya, A. O'Neill, S.D. Bergin, P.J. King, U. Khan, K. Young, A. Gaucher, S. De, R.J. Smith, I.V. Shvets, S.K. Arora, G. Stanton, H.-Y. Kim, K. Lee, G.T. Kim, G.S. Duesberg, T. Hallam, J.J. Boland, J.J. Wang, J.F. Donegan, J.C. Grunlan, G. Moriarty, A. Shmeliov, R.J. Nicholls, J.M. Perkins, E.M. Grieveson, K. Theuwissen, D.W. McComb, P.D. Nellist, V. Nicolosi, Science (80-.) 331 (2011) 568−571.

[31] V. Nicolosi, M. Chhowalla, M.G. Kanatzidis, M.S. Strano, J.N. Coleman, Science (80-.) 340 (2013), 1226419–1226419.

[32] J. Nevalaita, P. Koskinen, Nanoscale 11 (2019) 22019–22024.

[33] H. Häkkinen, M. Moseler, U. Landman, Phys. Rev. Lett. 89 (2002), 033401.

[34] X. Li, H. Zhai, L. Wang, H. Hakkinen, B. Yoon, U. Landman, J. Phys. Chem. (2003) 6168–6175.

[35] P. Koskinen, H. Häkkinen, G. Seifert, S. Sanna, T. Frauenheim, M. Moseler, New J. Phys. 8 (2006), 9–9.

[36] P. Koskinen, H. Häkkinen, B. Huber, B. von Issendorff, M. Moseler, Phys. Rev. Lett. 98 (2007), 015701.

[37] F. Furche, R. Ahlrichs, P. Weis, C. Jacob, S. Gilb, T. Bierweiler, M.M. Kappes, J. Chem. Phys. 117 (2002) 6982–6990.

[38] X. Zhao, J. Dan, J. Chen, Z. Ding, W. Zhou, K.P. Loh, S.J. Pennycook, Adv. Mater. 30 (2018) 1707281.

[39] P. Koskinen, T. Korhonen, Nanoscale 7 (2015) 10140–10145.

[40] J. Yuan, N. Yu, K. Xue, X. Miao, Appl. Surf. Sci. 409 (2017) 85–90.

[41] S. Zhang, M. Xie, F. Li, Z. Yan, Y. Li, E. Kan, W. Liu, Z. Chen, H. Zeng, Angew. Chem. Int. Ed. 55 (2016) 1666–1669.

[42] F. Ersan, E. Aktürk, S. Ciraci, Phys. Rev. B 94 (2016) 245417.

[43] C.-H. Hsu, Z.-Q. Huang, F.-C. Chuang, C.-C. Kuo, Y.-T. Liu, H. Lin, A. Bansil, New J. Phys. 17 (2015), 025005.

[44] L.-M. Yang, T. Frauenheim, E. Ganz, Phys. Chem. Chem. Phys. 17 (2015) 19695–19699.

[45] L.-M. Yang, M. Dornfeld, T. Frauenheim, E. Ganz, Phys. Chem. Chem. Phys. 17 (2015) 26036–26042.

[46] L.-M. Yang, T. Frauenheim, E. Ganz, J. Nanomater. 2016 (2016) 1–6.

[47] C. Kamal, A. Chakrabarti, M. Ezawa, New J. Phys. 17 (2015), 083014.

[48] V. Kochat, A. Samanta, Y. Zhang, S. Bhowmick, P. Manimunda, S.A.S. Asif, A.S. Stender, R. Vajtai, A.K. Singh, C.S. Tiwary, P.M. Ajayan, Sci. Adv. 4 (2018), e1701373.

[49] D. Singh, S.K. Gupta, I. Lukačević, M. Mužević, Y. Sonvane, R. Ahuja, Sci. Rep. 9 (2019) 17300.

[50] P. Rivero, J.-A. Yan, V.M. García-Suárez, J. Ferrer, S. Barraza-Lopez, Phys. Rev. B 90 (2014) 241408.

[51] B. Cai, S. Zhang, Z. Hu, Y. Hu, Y. Zou, H. Zeng, Phys. Chem. Chem. Phys. 17 (2015) 12634–12638.

[52] Y. Xu, B. Yan, H.-J. Zhang, J. Wang, G. Xu, P. Tang, W. Duan, S.-C. Zhang, Phys. Rev. Lett. 111 (2013) 136804.

[53] P. Tang, P. Chen, W. Cao, H. Huang, S. Cahangirov, L. Xian, Y. Xu, S.-C. Zhang, W. Duan, A. Rubio, Phys. Rev. B 90 (2014) 121408.

[54] F. Matusalem, M. Marques, L.K. Teles, F. Bechstedt, Phys. Rev. B 92 (2015), 045436.

[55] J. Nevalaita, P. Koskinen, Phys. Rev. B 97 (2018), 035411.

[56] F. Yang, L. Miao, Z.F. Wang, M.-Y. Yao, F. Zhu, Y.R. Song, M.-X. Wang, J.-P. Xu, A.V. Fedorov, Z. Sun, G.B. Zhang, C. Liu, F. Liu, D. Qian, C.L. Gao, J.-F. Jia, Phys. Rev. Lett. 109 (2012), 016801.

[57] Y. Lu, W. Xu, M. Zeng, G. Yao, L. Shen, M. Yang, Z. Luo, F. Pan, K. Wu, T. Das, P. He, J. Jiang, J. Martin, Y.P. Feng, H. Lin, X. Wang, Nano Lett. 15 (2015) 80–87.

[58] Y. Liu, N. Gao, J. Zhuang, C. Liu, J. Wang, W. Hao, S.X. Dou, J. Zhao, Y. Du, J. Phys. Chem. Lett. 10 (2019) 1558–1565.

[59] J. Yuhara, Y. Fujii, K. Nishino, N. Isobe, M. Nakatake, L. Xian, A. Rubio, G. Le Lay, 2D Mater. 5 (2018), 025002.

[60] S. Mardanya, V.K. Thakur, S. Bhowmick, A. Agarwal, Phys. Rev. B 94 (2016), 035423.

[61] D. Singh, S.K. Gupta, I. Lukačević, Y. Sonvane, RSC Adv. 6 (2016) 8006–8014.

[62] X.-L. Yu, L. Huang, J. Wu, Phys. Rev. B 95 (2017) 125113.

[63] E. Aktürk, O.Ü. Aktürk, S. Ciraci, Phys. Rev. B 94 (2016), 014115.

[64] S.A. Scott, M.V. Kral, S.A. Brown, Surf. Sci. 587 (2005) 175–184.

[65] J. Jiang, W. Ding, W. Li, Z. Wei, Inside Chem. 6 (2020) 431–447.

[66] D. Takimoto, W. Sugimoto, Q. Yuan, N. Takao, T. Itoh, T.V.T. Duy, T. Ohwaki, H. Imai, ACS Appl. Nano Mater. 2 (2019) 5743–5751.

[67] X. Kong, K. Xu, C. Zhang, J. Dai, S. Norooz Oliaee, L. Li, X. Zeng, C. Wu, Z. Peng, ACS Catal. 6 (2016) 1487–1492.

[68] M. Luo, Y. Yang, Y. Sun, Y. Qin, C. Li, Y. Li, M. Li, S. Zhang, D. Su, S. Guo, Mater. Today 23 (2019) 45–56.

[69] Y. Ma, B. Li, S. Yang, Mater. Chem. Front. 2 (2018) 456–457.

[70] S. Liu, H. Tao, L. Zeng, Q. Liu, Z. Xu, Q. Liu, J.-L. Luo, J. Am. Chem. Soc. 139 (2017) 2160–2163.

[71] L. Wang, Y. Zhu, J.-Q. Wang, F. Liu, J. Huang, X. Meng, J.-M. Basset, Y. Han, F.-S. Xiao, Nat. Commun. 6 (2015) 6957.

[72] H. Liu, P. Zhong, K. Liu, L. Han, H. Zheng, Y. Yin, C. Gao, Chem. Sci. 9 (2018) 398–404.

[73] X. Huang, S. Tang, X. Mu, Y. Dai, G. Chen, Z. Zhou, F. Ruan, Z. Yang, N. Zheng, Nat. Nanotechnol. 6 (2011) 28–32.

[74] Y. Zhao, S. Xing, X. Meng, J. Zeng, S. Yin, X. Li, Y. Chen, Nanoscale 11 (2019) 9319–9326.

[75] Y. Kang, Q. Xue, P. Jin, J. Jiang, J. Zeng, Y. Chen, ACS Sustain. Chem. Eng. 5 (2017) 10156–10162.

[76] Y. Zhang, D.E. Charles, D.M. Ledwith, D. Aherne, S. Cunningham, M. Voisin, W.J. Blau, Y.K. Gun'ko, J.M. Kelly, M.E. Brennan-Fournet, RSC Adv. 4 (2014) 29022–29031.

[77] Y.-T. (Frank) Pan, X. Yin, K.S. Kwok, H. Yang, Nano Lett. 14 (2014) 5953–5959.

[78] Y.-W. Jiang, G. Gao, P. Hu, J.-B. Liu, Y. Guo, X. Zhang, X.-W. Yu, F.-G. Wu, X. Lu, Nanoscale 12 (2020) 210–219.

[79] S. Tang, M. Chen, N. Zheng, Small 10 (2014) 3139–3144.

[80] Q. Zhang, Y. Hu, S. Guo, J. Goebl, Y. Yin, Nano Lett. 10 (2010) 5037–5042.

[81] H.L. Qin, D. Wang, Z.L. Huang, D.M. Wu, Z.C. Zeng, B. Ren, K. Xu, J. Jin, J. Am. Chem. Soc. 135 (2013) 12544–12547.

[82] A.-X. Yin, W.-C. Liu, J. Ke, W. Zhu, J. Gu, Y.-W. Zhang, C.-H. Yan, J. Am. Chem. Soc. 134 (2012) 20479–20489.

[83] M.A. Zeb Gul Sial, M.A. Ud Din, X. Wang, Chem. Soc. Rev. 47 (2018) 6175–6200.

[84] T.C.R. Rocha, D. Zanchet, J. Phys. Chem. C 111 (2007) 6989–6993.

[85] V. Germain, J. Li, D. Ingert, Z.L. Wang, M.P. Pileni, J. Phys. Chem. B 107 (2003) 8717–8720.

[86] Y. Xia, Y. Xiong, B. Lim, S.E. Skrabalak, Angew. Chem. Int. Ed. 48 (2009) 60–103.

[87] A. Courty, A.-I. Henry, N. Goubet, M.-P. Pileni, Nat. Mater. 6 (2007) 900–907.

[88] X. Huang, S.S.S. Li, Y. Huang, S. Wu, X. Zhou, S.S.S. Li, C.L. Gan, F. Boey, C.A. Mirkin, H. Zhang, Nat. Commun. 2 (2011) 292.

[89] M. Chhetri, M. Rana, B. Loukya, P.K. Patil, R. Datta, U.K. Gautam, Adv. Mater. 27 (2015) 4430–4437.

[90] H. Liu, H. Tang, M. Fang, W. Si, Q. Zhang, Z. Huang, L. Gu, W. Pan, J. Yao, C. Nan, H. Wu, Adv. Mater. 28 (2016) 8170–8176.

[91] G. Wu, X. Zheng, P. Cui, H. Jiang, X. Wang, Y. Qu, W. Chen, Y. Lin, H. Li, X. Han, Y. Hu, P. Liu, Q. Zhang, J. Ge, Y. Yao, R. Sun, Y. Wu, L. Gu, X. Hong, Y. Li, Nat. Commun. 10 (2019) 4855.

[92] T. Wang, Q. He, J. Zhang, Z. Ding, F. Li, Y. Yang, Mater. Today 36 (30) (2020).

[93] Z. Fan, M. Bosman, X. Huang, D. Huang, Y. Yu, K.P. Ong, Y.A. Akimov, L. Wu, B. Li, J. Wu, Y. Huang, Q. Liu, C. Eng Png, C. Lip Gan, P. Yang, H. Zhang, Nat. Commun. 6 (2015) 7684.

[94] S. Gao, Y. Lin, X. Jiao, Y. Sun, Q. Luo, W. Zhang, D. Li, J. Yang, Y. Xie, Nature 529 (2016) 68–71.

[95] J.-W. Yu, X.-Y. Wang, C.-Y. Yuan, W.-Z. Li, Y.-H. Wang, Y.-W. Zhang, Nanoscale 10 (2018) 6936–6944.

[96] C. He, J. Tao, P.K. Shen, ACS Catal. 8 (2018) 910–919.

[97] M. Chen, B. Wu, J. Yang, N. Zheng, Adv. Mater. 24 (2012) 862–879.

[98] J. Zeng, X. Xia, M. Rycenga, P. Henneghan, Q. Li, Y. Xia, Angew. Chem. Int. Ed. 50 (2011) 244–249.

[99] Y. Xiong, I. Washio, J. Chen, H. Cai, Z.-Y. Li, Y. Xia, Langmuir 22 (2006) 8563–8570.

[100] Y. Huang, A.R. Ferhan, Y. Gao, A. Dandapat, D.-H.H. Kim, Nanoscale 6 (2014) 6496–6500.

[101] D. Xu, X. Liu, H. Lv, Y. Liu, S. Zhao, M. Han, J. Bao, J. He, B. Liu, Chem. Sci. 9 (2018) 4451–4455.

[102] H. Duan, N. Yan, R. Yu, C.-R. Chang, G. Zhou, H.-S. Hu, H. Rong, Z. Niu, J. Mao, H. Asakura, T. Tanaka, P.J. Dyson, J. Li, Y. Li, Nat. Commun. 5 (2014) 3093.

[103] Z. Fan, X. Huang, Y. Han, M. Bosman, Q. Wang, Y. Zhu, Q. Liu, B. Li, Z. Zeng, J. Wu, W. Shi, S. Li, C.L. Gan, H. Zhang, Nat. Commun. 6 (2015) 6571.

[104] Q. Zhang, N. Li, J. Goebl, Z. Lu, Y. Yin, J. Am. Chem. Soc. 133 (2011) 18931–18939.

[105] J. Niu, D. Wang, H. Qin, X. Xiong, P. Tan, Y. Li, R. Liu, X. Lu, J. Wu, T. Zhang, W. Ni, J. Jin, Nat. Commun. 5 (2014) 3313.

[106] H. Zhao, J. Wu, H. You, S. Yang, B. Ding, Z. Yang, X. Song, H. Yang, J. Mater. Chem. 22 (2012) 12046.

[107] Y. Kuang, G. Feng, P. Li, Y. Bi, Y. Li, X. Sun, Angew. Chem. Int. Ed. 55 (2016) 693–697.

[108] A.H. Shaik, J. Chakraborty, RSC Adv. 6 (2016) 14952–14957.

[109] G. Lin, W. Lu, W. Cui, L. Jiang, Cryst. Growth Des. 10 (2010) 1118–1123.

[110] S. Porel, S. Singh, T.P. Radhakrishnan, Chem. Commun. (2005) 2387.

[111] Y. Zhai, J.S. DuChene, Y.-C. Wang, J. Qiu, A.C. Johnston-Peck, B. You, W. Guo, B. DiCiaccio, K. Qian, E.W. Zhao, F. Ooi, D. Hu, D. Su, E.A. Stach, Z. Zhu, W.D. Wei, Nat. Mater. 15 (2016) 889–895.

[112] G.S. Métraux, C.A. Mirkin, Adv. Mater. 17 (2015), 2685–2685.

[113] I. Washio, Y. Xiong, Y. Yin, Y. Xia, Adv. Mater. 18 (2006) 1745–1749.

[114] C.S. Ah, Y.J. Yun, H.J. Park, W.-J. Kim, D.H. Ha, W.S. Yun, Chil Seong Ah, Yong Ju Yun, Hyung Ju Park, Wan-Joong Kim, A. Dong Han Ha, W.S. Yun*, Chem. Mater. 17 (2005) 5558–5561.

[115] R. Fu, S. Xu, Y.-N. Lu, J.-J. Zhu, Cryst. Growth Des. 5 (2005) 1379–1385.

[116] I. Pastoriza-Santos, L.M. Liz-Marzán, Nano Lett. 2 (2002) 903–905.

[117] N. Yang, Z. Zhang, B. Chen, Y. Huang, J. Chen, Z. Lai, Y. Chen, M. Sindoro, A.-L.A. Wang, H. Cheng, Z. Fan, X. Liu, B. Li, Y. Zong, L. Gu, H. Zhang, Adv. Mater. 29 (2017) 1700769.

[118] I. Pastoriza-Santos, A. Sánchez-Iglesias, B. Rodríguez-González, L.M. Liz-Marzán, Small 5 (2009) 440–443.

[119] Q. Li, F. Liu, C. Lu, J.-M. Lin, J. Phys. Chem. C 115 (2011) 10964–10970.

[120] C. Salzemann, J. Urban, I. Lisiecki, M.-P. Pileni, Adv. Funct. Mater. 15 (2005) 1277–1284.

[121] T.H. Ha, Y.J. Kim, S.H. Park, Chem. Commun. 46 (2010) 3164.

[122] M.H. Kim, D.K. Yoon, S.H. Im, RSC Adv. 5 (2015) 14266–14272.

[123] K. Jang, H.J. Kim, S.U. Son, Chem. Mater. 22 (2010) 1273–1275.

[124] H. Lv, H. Sun, D. Xu, S.L. Suib, B. Liu, Green Chem. 21 (2019) 2367–2374.

[125] H. Guo, Y. Chen, H. Ping, L. Wang, D.-L. Peng, J. Mater. Chem. 22 (2012) 8336–8344.

[126] D. Xu, H. Lv, H. Jin, Y. Liu, Y. Ma, M. Han, J. Bao, B. Liu, J. Phys. Chem. Lett. 10 (2019) 663–671.

[127] H. Wang, X. He, Y. Zhao, J. Li, T. Huang, H. Liu, CrystEngComm 19 (2017) 4304–4311.
[128] J.S. DuChene, W. Niu, J.M. Abendroth, Q. Sun, W. Zhao, F. Huo, W.D. Wei, Chem. Mater. 25 (2013) 1392–1399.
[129] M.H. Kim, S.K. Kwak, S.H. Im, J.-B. Lee, K.-Y. Choi, D.-J. Byun, J. Mater. Chem. C 2 (2014) 6165–6170.
[130] H. Li, G. Chen, H. Yang, X. Wang, J. Liang, P. Liu, M. Chen, N. Zheng, Angew. Chem. Int. Ed. 52 (2013) 8368–8372.
[131] Y. Li, Y. Yan, Y. Li, H. Zhang, D. Li, D. Yang, CrystEngComm 17 (2015) 1833–1838.
[132] Z. Wang, Y. Chen, D. Zeng, Q. Zhang, D.-L. Peng, CrystEngComm 18 (2016) 1295–1301.
[133] P.F. Siril, L. Ramos, P. Beaunier, P. Archirel, A. Etcheberry, H. Remita, Chem. Mater. 21 (2009) 5170–5175.
[134] J.W. Hong, Y. Kim, D.H. Wi, S. Lee, S.-U. Lee, Y.W. Lee, S.-I. Choi, S.W. Han, Angew. Chem. Int. Ed. 55 (2016) 2753–2758.
[135] M. Shirai, K. Igeta, M. Arai, Chem. Commun. (2000) 623–624.
[136] J. Walter, J. Heiermann, G. Dyker, S. Hara, H. Shioyama, J. Catal. 189 (2000) 449–455.
[137] X. Lv, X. Li, C. Yang, X. Ding, Y. Zhang, Y. Zheng, S. Li, X. Sun, X. Tao, Adv. Funct. Mater. 1910830 (2020) 1910830.
[138] C. Lee, E.A. Josephs, J. Shao, T. Ye, J. Phys. Chem. C 116 (2012) 17625–17632.
[139] Y. Jiang, Y. Yan, W. Chen, Y. Khan, J. Wu, H. Zhang, D. Yang, Chem. Commun. 52 (2016) 14204–14207.
[140] X. Huang, H. Li, S. Li, S. Wu, F. Boey, J. Ma, H. Zhang, Angew. Chem. Int. Ed. 50 (2011) 12245–12248.
[141] J. Walter, Adv. Mater. 12 (2000) 31–33.
[142] J. Gu, B. Li, Z. Du, C. Zhang, D. Zhang, S. Yang, Adv. Funct. Mater. 27 (2017) 1700840.
[143] N. Hussain, T. Liang, Q. Zhang, T. Anwar, Y. Huang, J. Lang, K. Huang, H. Wu, Small 13 (2017) 1701349.
[144] K. Huang, J. Hou, Q. Zhang, G. Ou, D. Ning, N. Hussain, Y. Xu, B. Ge, K. Liu, H. Wu, Chem. Commun. 54 (2017) 160–163.
[145] A. Funatsu, H. Tateishi, K. Hatakeyama, Y. Fukunaga, T. Taniguchi, M. Koinuma, H. Matsuura, Y. Matsumoto, Chem. Commun. 50 (2014) 8503–8506.
[146] L. Zeng, C. You, N. Hong, X. Zhang, T. Liang, Adv. Eng. Mater. 22 (2020) 1901359.
[147] K. Fukuda, J. Sato, T. Saida, W. Sugimoto, Y. Ebina, T. Shibata, M. Osada, T. Sasaki, Inorg. Chem. 52 (2013) 2280–2282.
[148] J. Gu, Z. Du, C. Zhang, J. Ma, B. Li, S. Yang, Adv. Energy Mater. 7 (2017) 1700447.
[149] Phil. Trans. Roy. Soc. Lond. 147 (1857) 145–181.
[150] X. Huang, X. Zhou, S. Wu, Y. Wei, X. Qi, J. Zhang, F. Boey, H. Zhang, Small 6 (2010) 513–516.
[151] J.S. Huang, V. Callegari, P. Geisler, C. Brüning, J. Kern, J.C. Prangsma, X. Wu, T. Feichtner, J. Ziegler, P. Weinmann, M. Kamp, A. Forchel, P. Biagioni, U. Sennhauser, B. Hecht, Nat. Commun. 1 (2010).
[152] L. Zhang, C.Z. Huang, Y.F. Li, Q. Li, Cryst. Growth Des. 9 (2009) 3211–3217.
[153] T.H. Ha, H.-J. Koo, B.H. Chung, J. Phys. Chem. C 111 (2007) 1123–1130.
[154] M. Chen, D.W. Goodman, Acc. Chem. Res. 39 (2006) 739–746.
[155] J.E. Millstone, G.S. Métraux, C.A. Mirkin, Adv. Funct. Mater. 16 (2006) 1209–1214.
[156] X. Sun, S. Dong, E. Wang, Langmuir 21 (2005) 4710–4712.
[157] X. Sun, S. Dong, E. Wang, Angew. Chem. Int. Ed. 43 (2004) 6360–6363.
[158] W. Zang, J. Toster, B. Das, R. Gondosiswanto, S. Liu, P.K. Eggers, C. Zhao, C.L. Raston, X. Chen, Chem. Commun. 55 (2019) 3785–3788.
[159] L. Lv, X. Wu, Y. Yang, X. Han, R. Mezzenga, C. Li, ACS Sustain. Chem. Eng. 6 (2018) 12419–12425.
[160] L. Bi, J. Dong, W. Xie, W. Lu, W. Tong, L. Tao, W. Qian, Anal. Chim. Acta 805 (2013) 95–100.
[161] B. Cao, B. Liu, J. Yang, CrystEngComm 15 (2013) 5735.
[162] B. Pelaz, V. Grazu, A. Ibarra, C. Magen, P. del Pino, J.M. de la Fuente, Langmuir 28 (2012) 8965–8970.
[163] K. Banu, T. Shimura, New J. Chem. 36 (2012) 2112–2120.
[164] S. Hong, Y. Choi, S. Park, Chem. Mater. 23 (2011) 5375–5378.
[165] S.-W. Lee, K.-S. Lee, J. Ahn, J.-J. Lee, M.-G. Kim, Y.-B. Shin, ACS Nano 5 (2011) 897–904.
[166] J. Song, Y. Chu, Y. Liu, L. Li, W. Sun, Chem. Commun. (2008) 1223.
[167] Z. Deng, M. Mansuipur, A.J. Muscat, J. Phys. Chem. C 113 (2009) 867–873.
[168] M. Liu, M. Leng, C. Yu, X. Wang, C. Wang, Nano Res 3 (2010) 843–851.
[169] N. Cathcart, V. Kitaev, ACS Nano 5 (2011) 7411–7425.
[170] M.M. Shahjamali, M. Bosman, S. Cao, X. Huang, S. Saadat, E. Martinsson, D. Aili, Y.Y. Tay, B. Liedberg, S.C.J. Loo, H. Zhang, F. Boey, C. Xue, Adv. Funct. Mater. 22 (2012) 849–854.
[171] X. Liu, L. Li, Y. Yang, Y. Yin, C. Gao, Nanoscale 6 (2014) 4513–4516.
[172] S. Chen, D.L. Carroll, Nano Lett. 2 (2002) 1003–1007.
[173] M. Maillard, S. Giorgio, M.-P. Pileni, J. Phys. Chem. B 107 (2003) 2466–2470.
[174] A.J. Haes, J. Zhao, S. Zou, C.S. Own, L.D. Marks, G.C. Schatz, R.P. Van Duyne, J. Phys. Chem. B 109 (2005) 11158–11162.
[175] V. Bastys, I. Pastoriza-Santos, B. Rodríguez-González, R. Vaisnoras, L.M. Liz-Marzán, Adv. Funct. Mater. 16 (2006) 766–773.
[176] Y. Xiong, J. Washio, J. Chen, M. Sadilek, Y. Xia, Angew. Chem. 119 (2007) 5005–5009.
[177] D. Aherne, D.M. Ledwith, M. Gara, J.M. Kelly, Adv. Funct. Mater. 18 (2008) 2005–2016.
[178] X. Yin, X. Liu, Y.-T. Pan, K.A. Walsh, H. Yang, Nano Lett. 14 (2014) 7188–7194.
[179] Y. Zhang, M. Wang, E. Zhu, Y. Zheng, Y. Huang, X. Huang, Nano Lett. 15 (2015) 7519–7525.
[180] D. Xu, Y. Liu, S. Zhao, Y. Lu, M. Han, J. Bao, Chem. Commun. 53 (2017) 1642–1645.
[181] X. Lou, H. Pan, S. Zhu, C. Zhu, Y. Liao, Y. Li, D. Zhang, Z. Chen, Catal. Commun. 69 (2015) 43–47.
[182] S. Yang, P. Qiu, G. Yang, Carbon N. Y. 77 (2014) 1123–1131.
[183] G. Liu, W. Zhou, B. Chen, Q. Zhang, X. Cui, B. Li, Z. Lai, Y. Chen, Z. Zhang, L. Gu, H. Zhang, Nanomater. Energy 66 (2019) 104173.
[184] R.M. Garcia, Y. Song, R.M. Dorin, H. Wang, A.M. Moreno, Y.-B. Jiang, Y. Tian, Y. Qiu, C.J. Medforth, E.N. Coker, F. van Swol, J.E. Miller, J.A. Shelnutt, Phys. Chem. Chem. Phys. 13 (2011) 4846–4852.
[185] K. Kusada, H. Kobayashi, T. Yamamoto, S. Matsumura, N. Sumi, K. Sato, K. Nagaoka, Y. Kubota, H. Kitagawa, J. Am. Chem. Soc. 135 (2013) 5493–5496.
[186] X. Huang, Z. Zeng, S. Bao, M. Wang, X. Qi, Z. Fan, H. Zhang, Nat. Commun. 4 (2013).
[187] H. Aharoni, D.V. Todorova, O. Albarrán, L. Goehring, R.D. Kamien, E. Katifori, Nat. Commun. 8 (2017) 15809.
[188] Z. Chen, G. Huang, I. Trase, X. Han, Y. Mei, Phys. Rev. Appl. 5 (2016), 017001.
[189] H. Vandeparre, S. Desbief, R. Lazzaroni, C. Gay, P. Damman, Soft Matter 7 (2011) 6878–6882.
[190] J.Y. Zhang, Z.Y. Ding, F.C. Li, Y. Yang, Nanotechnology 31 (2020), 045601.
[191] I. Petrov, P.B. Barna, L. Hultman, J.E. Greene, J. Vac. Sci. Technol. A Vacuum, Surfaces, Film. 21 (2003) S117–S128.
[192] J.W. Abraham, T. Strunskus, F. Faupel, M. Bonitz, J. Appl. Phys. 119 (2016) 185301.
[193] Y.Y. Lu, R. Kotoka, J.P. Ligda, B.B. Cao, S.N. Yarmolenko, B.E. Schuster, Q. Wei, Acta Mater. 63 (2014) 216–231.
[194] J.Y. Zhang, Y. Liu, J. Chen, Y. Chen, G. Liu, X. Zhang, J. Sun, Mater. Sci. Eng. A 552 (2012) 392–398.
[195] S.V. Ketov, Y.P. Ivanov, D. Şopu, D.V. Louzguine-Luzgin, C. Suryanarayana, A.O. Rodin, T. Schöberl, A.L. Greer, J. Eckert, Mater. Today Adv. 1 (2019) 100004.
[196] Z. Fan, X. Huang, C. Tan, H. Zhang, Chem. Sci. 6 (2015) 95–111.
[197] S. Tang, X. Huang, N. Zheng, Chem. Commun. 47 (2011) 3948–3950.
[198] G.P. Luke, A. Bashyam, K.A. Homan, S. Makhija, Y.-S. Chen, S.Y. Emelianov, Nanotechnology 24 (2013) 455101.
[199] M. Chen, S. Tang, Z. Guo, X. Wang, S. Mo, X. Huang, G. Liu, N. Zheng, Adv. Mater. 26 (2014) 8210–8216.
[200] C. Bao, N. Beziere, P. del Pino, B. Pelaz, G. Estrada, F. Tian, V. Ntziachristos, J.M. de la Fuente, D. Cui, Small 9 (2013) 68–74.
[201] D. Deng, K.S. Novoselov, Q. Fu, N. Zheng, Z. Tian, X. Bao, Nat. Nanotechnol. 11 (2016) 218–230.
[202] S. Rusponi, T. Cren, N. Weiss, M. Epple, P. Buluschek, L. Claude, H. Brune, Nat. Mater. 2 (2003) 546–551.
[203] R. Xu, T. Xie, Y. Zhao, Y. Li, Cryst. Growth Des. 7 (2007) 1904–1911.
[204] L.R. Hirsch, R.J. Stafford, J.A. Bankson, S.R. Sershen, B. Rivera, R.E. Price, J.D. Hazle, N.J. Halas, J.L. West, Proc. Natl. Acad. Sci. Unit. States Am. 100 (2003) 13549–13554.
[205] C. Gao, Z. Lu, Y. Liu, Q. Zhang, M. Chi, Q. Cheng, Y. Yin, Angew. Chem. Int. Ed. 51 (2012) 5629–5633.
[206] G. Barbillon, J.-L. Bijeon, J. Plain, P. Royer, Thin Solid Films 517 (2009) 2997–3000.
[207] E.M. Larsson, J. Alegret, M. Käll, D.S. Sutherland, Nano Lett. 7 (2007) 1256–1263.
[208] Y.N. Wijaya, J. Kim, W.M. Choi, S.H. Park, M.H. Kim, Nanoscale 9 (2017) 11705–11712.
[209] W. Wang, Y. Zhao, Y. Ding, Nanoscale 7 (2015) 11934–11939.
[210] L. Dai, Y. Zhao, Q. Qin, X. Zhao, C. Xu, N. Zheng, ChemNanoMat 2 (2016) 776–780.
[211] F. Saleem, Z. Zhang, B. Xu, X. Xu, P. He, X. Wang, J. Am. Chem. Soc. 135 (2013) 18304–18307.
[212] M. Du, L. Cui, Y. Cao, A.J. Bard, J. Am. Chem. Soc. 137 (2015) 7397–7403.
[213] K. Wang, Y. Qin, F. Lv, M. Li, Q. Liu, F. Lin, J. Feng, C. Yang, P. Gao, S. Guo, Small Methods 2 (2018) 1700331.
[214] Q. Yang, L. Shi, B. Yu, J. Xu, C. Wei, Y. Wang, H. Chen, J. Mater. Chem. 7 (2019) 18846–18851.
[215] A. Mahmood, H. Lin, N. Xie, X. Wang, Chem. Mater. 29 (2017) 6329–6335.
[216] Y. Chen, X.X. Zheng, X.Y. Huang, A.J. Wang, Q.L. Zhang, H. Huang, J.J. Feng, J. Colloid Interface Sci. 559 (2020) 206–214.
[217] L. Dai, Q. Qin, P. Wang, X. Zhao, C. Hu, P. Liu, R. Qin, M. Chen, D. Ou, C. Xu, Sci. Adv. 3 (2017), e1701069.
[218] Y. Pi, N. Zhang, S. Guo, J. Guo, X. Huang, Nano Lett. 16 (2016) 4424–4430.
[219] Z. Ding, J. Bian, S. Shuang, X. Liu, Y. Hu, C. Sun, Y. Yang, Adv. Sustain. Syst. 4 (2020) 1900105.
[220] F. Saleem, B. Xu, B. Ni, H. Liu, F. Nosheen, H. Li, X. Wang, Adv. Mater. 27 (2015) 2013–2018.
[221] A. Mahmood, F. Saleem, H. Lin, B. Ni, X. Wang, Chem. Commun. 52 (2016) 10547–10550.
[222] T. Ling, J.J. Wang, H. Zhang, S.T. Song, Y.Z. Zhou, J. Zhao, X.W. Du, Adv. Mater. 27 (2015) 5396–5402.
[223] Y. Leng, Y. Zhang, T. Liu, M. Suzuki, X. Li, Nanotechnology 17 (2006) 1797.
[224] Y. Leng, Y. Wang, X. Li, T. Liu, S. Takahashhi, Nanotechnology 17 (2006) 4834.
[225] Z. Liu, S. Li, Y. Yang, S. Peng, Z. Hu, Y. Qian, Adv. Mater. 15 (2003) 1946–1948.

[226] O. Hjortstam, J. Trygg, J.M. Wills, B. Johansson, O. Eriksson, Phys. Rev. B 53 (1996) 9204.

[227] J. Izquierdo, A. Vega, L.C. Balbás, D. Sánchez-Portal, J. Junquera, E. Artacho, J.M. Soler, P. Ordejón, Phys. Rev. B 61 (2000) 13639.

[228] M.A. Meitl, Z.-T. Zhu, V. Kumar, K.J. Lee, X. Feng, Y.Y. Huang, I. Adesida, R.G. Nuzzo, J.A. Rogers, Nat. Mater. 5 (2006) 33–38.

[229] J.-H. Ahn, H.-S. Kim, K.J. Lee, S. Jeon, S.J. Kang, Y. Sun, R.G. Nuzzo, J.A. Rogers, Science 314 (2006) 1754–1757.

[230] S. Zhang, Z. Yan, Y. Li, Z. Chen, H. Zeng, Angew. Chem. Int. Ed. 54 (2015) 3112–3115.